



Post-glacial reshaping of Alpine topography induced by landsliding

2

1

Coline Ariagno^{1,2}, Philippe Steer¹, Pierre G. Valla², Benjamin Campforts³

5 6 7

8

¹Université Rennes, Géosciences

²ISTerre, Grenoble CNRS

³ Department of Earth Sciences, VU University Amsterdam, Netherlands

Correspondence to: Coline Ariagno (coline.ariagno@unive-rennes.fr)

14

15

16

17

18

19 20

21

22

23

24

25

26 27

28

29

30

31

32

33

34

35

36

37

Abstract. In steep alpine environments, successive glacial-interglacial cycles during the Quaternary led to multiple transient geomorphological phases. In particular, post-glacial periods are key transition phases experiencing rapid geomorphic changes, characterized by intense hillslope processes where ice and permafrost have retreated. Mass wasting is the dominant post-glacial process driving sediment production in steep mountain landscapes. However, its role in shaping topography, particularly in comparison to glacial activity—known for its strong deformational impact—remains poorly understood. By integrating numerical modeling with topographic data, we refine our understanding of how mass wasting shapes evolving landscape and influences sediment dynamics. In the Ecrins massif (French western Alps), we select three catchments, with particular morphological signatures or inheritance (i.e. from fluvial to glacial) to model their associated topographic evolution driven by mass wasting. Using the landscape evolution model 'HyLands', we quantitatively assess their individual response to landsliding by exploring the role of different internal or external factors (e.g., bedrock cohesion, return time of landslides). The model is calibrated with the output landslide area-volume scaling law and the massif-averaged denudation rate, inferred from literature. We focus on the cumulative impact of landslides, over a single post-glacial period, on catchment slope distribution, hypsometry, produced sediment volume and erosion rate. Compared to fluvial ones, inherited glacial topography shows a bimodal distribution of elevation for unstable slopes, near the crests and along the U-shape valley walls. The time evolution of this distribution is characterized by a decrease in the number of unstable slopes as well as a lowering in maximum catchment elevations induced by landsliding, usually attributed to the glacial buzzsaw. Indeed, glaciers may be not the only agent controlling mountain elevation, as we discussed in this study. Despite the stochastic nature of landslides, our modeling results also show that landslide activity and induced erosion rates are maximum at the onset of the glacial retreat and then progressive decay during the interglacial period. On the contrary, fluvial catchments show a more stable topography and less intense landslide activity resulting in lower erosion rates. This study quantitatively explores the non-linear interactions between landslides and catchment topographic evolution and questions the role of landslides in the erosion pulse during the Quaternary interglacial periods.





1. Introduction

41 The Quaternary period is characterized by oscillations from glacial to interglacial cycles overprinting a global climatic cooling trend over the Cenozoic era (Zachos et al., 2001). These successive climatic 42 transitions have been suggested to be associated with abrupt and transient geomorphologic and 43 44 topographic changes (Champagnac et al., 2014; Peizhen et al., 2001). In high-latitude regions and 45 mountain ranges, glaciers are usually considered as the main geomorphic and erosion agents (Hallet et al., 1996; Herman et al., 2013, 2021; Herman & Champagnac, 2016; Métivier et al., 1999). The 46 47 topographic changes resulting from glacial erosion are progressive and spatially variable over a single or multiple glacial-interglacial cycle (Seguinot & Delaney, 2021) of the Quaternary (Herman et al., 48 49 2011; Pedersen & Egholm, 2013; Sternai et al., 2013; Tomkin & Braun, 2002). Glaciated landscapes have in turn been widely studied to better understand past glacier dynamics and quantify glacial erosion 50 51 rates and associated topographic changes at the Earth's surface (Ganti et al., 2016; M. Koppes et al., 52 2015; Pedersen & Egholm, 2013; Peizhen et al., 2001; Solomina et al., 2015; Sternai et al., 2013). 53 Glacial and periglacial processes have strongly imprinted mountainous landforms, shaping U-shaped 54 valleys, but also cirques, arêtes and hanging valleys, all characterized by steep slopes and rugged topography (e.g. Anderson et al., 2006; Penck, 1905; Prasicek et al., 2015). In turn, glacial 55 56 morphological features likely represent transient and mechanically unstable landforms under interglacial 57 conditions (Herman & Braun, 2008; Prasicek et al., 2015), dominated by hillslope and fluvial processes. 58 Understanding the interglacial evolution of formerly glaciated landscapes has remained challenging 59 since it involves complex non-linear geomorphic processes and interrelated spatial/temporal scales. Yet, 60 this is a major need for assessing the ongoing response of mountainous environments to current climate 61 warming (e.g. Zhang et al., 2022). Interglacial periods are associated with overall warming climatic conditions, leading to a progressive 62 cryosphere degradation (i.e. glacier retreat and permafrost recession), and in turn to a shift of the main 63 64 geomorphic and erosion processes. Under interglacial conditions, paraglacial (Ballantyne, 2002) and 65 periglacial (French, 2017) processes become more efficient and affect larger mountainous areas. 66 Hillslope processes, including landsliding, rockfall and soil creep, affect formerly glaciated mountain 67 slopes. Rivers transport remobilized and newly-produced sediments (Roussel et al., 2018) and can 68 locally re-incise glacial valleys (e.g. Leith et al., 2018; Valla et al., 2010). Over the Quaternary, repetitive 69 climatic oscillations between glacial and interglacial periods have caused frequent mismatches between 70 dominant geomorphological processes and the organization or shape of the landscape on which they act. 71 This has led to the hypothesis that these transient climatic/geomorphic conditions over the Quaternary 72 could have led to an increase in erosion, sediment flux (M. Koppes et al., 2015; M. N. Koppes & Montgomery, 2009; Peizhen et al., 2001) and topographic relief (Champagnac et al., 2014), rather than 73 74 the supposed greater efficiency of glacial erosion itself (Koppes and Montgomery, 2009).



76

77

78 79

80

81 82

83

84

85

86 87

88

89

90

91 92

93

94

95 96

97

98

99

100

101

102

103

104

105

106107

108

109

110



In the following work, we focus on the transient phase from glacial to interglacial conditions, hereinafter referred to as the post-glacial period, i.e. when alpine glaciers retreated and left uncovered landscape dominated by non-glacial geomorphic agents. In this context, steep parts of mountain hillslopes become more prone to mass wasting processes, favored by glacial debuttressing (E. Cossart et al., 2008) and permafrost retreat (e.g. Cathala et al., 2024; Lebrouc et al., 2013). The rapid climate change observed over the last decades has motivated research on the evolution of permafrost and its impact on highelevation rockwall dynamics (Gallach et al., 2020; Magnin et al., 2017; Ravanel et al., 2017; Stoffel et al., 2024). In addition, gravitational instabilities, such as bedrock landslides or rockfalls, are widespread in mountainous landscapes and appear as one of the most efficient processes to shape them (Keefer, 1984). Taking over glacial erosion, hillslope activity transiently reshapes glacial morphological features leading to a postglacial increase in both the frequency and intensity of hillslope events through time (e.g. Korup, 2006; Zerathe et al., 2014). Landslides significantly contribute to catchment-scale erosion by mobilizing large bedrock volumes, which greatly impact sediment fluxes (Broeckx et al., 2020; Hovius et al., 1997; Zech et al., 2009). As a positive feedback loop, by decreasing the local baselevel, fluvial sediment export and incision of formerly glaciated valleys, can foster the hillslope response. The postglacial period is also associated to major changes in the hillslope-channel connectivity (Brardinoni & Hassan, 2007; Cavalli et al., 2019; Müller et al., 2022) and in the drainage system (Comiti et al., 2019; Lane et al., 2017; Pitlick et al., 2021; Zhang et al., 2022). As such, this period appears complex due to rapid morphological changes and multiple geomorphic processes that all interact and drive major changes in both the hillslope domain and the drainage network. Therefore, quantifying the spatiotemporal impact of landslides on evolving postglacial landscapes is needed to better understand sediment production, transfer and potential storage along the source to sink pathway and assess the overall topographic evolution in mountainous environments. If the landsliding impact on mountain topography appears clear after a single triggering event, such as a storm or an earthquake (Dahlquist et al., 2018; Meunier et al., 2008; Morriss et al., 2023; J. Roering, 2012), their role in long-term shaping of mountain range is not straightforward. For investigating the post-glacial period, landslide catalogues (Blondeau et al., 2021; Wood et al., 2015), bedload records (Lane et al., 2017), remote-sensing and geophysical methods have intrinsic limitations and integration times that are too short. Conversely, long-term mountain erosion estimates from geochronological and thermochronological methods (Herman et al., 2013) or large-scale sediment budgets (Kuhlemann et al., 2002) may have too long integration times to investigate interglacial periods. Terrestrial cosmogenic nuclides (TCN) have been commonly used to quantify catchment-wide erosion rates over $10^2 - 10^5$ yr timescales (Brown et al., 1995; Delunel et al., 2020; Mudd et al., 2016; Portenga & Bierman, 2011), covering glacial-interglacial cycles. Although this approach appears meaningful to address the postglacial period (~10-20 kyr), TCN-derived erosion rates are punctual and averaged in both space (catchment) and time. In turn, this prevents exploring in detail the spatial distribution and temporal





111 evolution of erosion during that period. Moreover, the cosmic ray attenuation depth, which sets the 112 integration time of TCN (von Blanckenburg, 2005), can be significantly smaller than the depth of large to gigantic landslides observed in formerly glaciated catchments (Korup, 2006; Lavé et al., 2023). 113 Overall, this raises the question of the potential limitations of TCN-derived erosion rates in constraining 114 the time evolution of post-glacial erosion in landscapes dominated by bedrock landsliding. 115 116 In this context, landscape evolution modelling (LEM) appears as a relevant approach to overcome the 117 limited amount of data/observations and the intertwined spatial and temporal scales involved (Tucker & 118 Hancock, 2010). Numerical modelling can combine complex surface processes, including tectonic 119 uplift, hillslope and river dynamics integrating all the sediment transfer cascade and hillslope-channel 120 connectivity, while allowing predictions over large spatial and temporal scales. Different categories of 121 models can be considered to study mass wasting processes (Campforts et al., 2022). Physical-based 122 models produce realistic debris-flow (and river) propagation and deposition but may not be adapted for 123 large-scale landscape evolution (Croissant et al., 2017; Davy et al., 2017; Dietrich et al., 1995; George 124 & Iverson, 2014; Hergarten & Robl, 2015; Martin et al., 2023). Landscape evolution models (LEM) 125 rather use reduced-complexity geomorphic laws to simulate the evolution topography over possibly long 126 timescales and large spatial scales (Carriere et al., 2020; Langston & Tucker, 2018; Liebl et al., 2021). 127 For instance, linear or non-linear diffusion laws are generally used to simulate hillslope erosion in most 128 LEMs (Heimsath et al., 2005; Perron, 2011; J. J. Roering et al., 1999). Soil-covered models simulate 129 shallow landslides to follow for instance the impact of rainfall variability at large scale (Claessens et al., 130 2007), while bedrock-landslide models allow the distinction between constant and episodic sediment production through landslides (Campforts et al., 2020; Densmore et al., 1998). Therefore, numerical 131 132 modelling offers multiple ways to simulate hillslopes processes, and their interactions, by highlighting diverse approaches, modeling complexity and spatio-temporal scales. 133 134 The aim of this study is to explore numerically, using a reduced-complexity model, the role of landslides in the postglacial morphological dynamics of mountainous landscapes. We use the HyLands model 135 136 (Campforts et al., 2020, 2022), which explicitly simulate bedrock landslides, to predict associated mass 137 redistribution and the resulting catchment-averaged erosion rates and topographic evolution through 138 multiple timescales. We investigated the topographic impact of landslide activity on selected Alpine 139 catchments, located in the Ecrins massif (France), showcasing a gradient of glacial imprint and 140 deglaciation timing. An open question is the role of interglacial processes in erasing the inherited 141 morphological signature of former glaciation, leading to an erosional "hot-moment". More specifically, 142 we aim to assess the timescales, rates and locations of topographic changes associated with the transient 143 shift from glacial to interglacial periods, with a particular focus on the role of landsliding. Our working 144 hypothesis is that the different morphological signatures observed for Alpine catchments are evidencing 145 both landslide activity and deglaciation timing. The first objective of the study is to conduct a spatial 146 analysis of simulated landslides to assess their magnitudes and locations within investigated catchments.





Then, a temporal analysis is performed to investigate whether the postglacial period remains a transient phase and how long it may require to achieve an interglacial steady-state topography and erosion dynamics under landslide activity.

150

151

152

153

154

155

156

157158

159

160

161

162163

164

165

166

167

168169

170

171

172173

174

175

176

177

178

2. Study area

2.1 Tree selected catchments in the Ecrins massif

The Ecrins massif (south-east France, Fig. 1A) forms a high-elevation high-relief area of the southwestern Alps, and today still hosts glaciers in its upper catchments. The present-day topography was deeply impacted by glaciation (van der Beek & Bourbon, 2008), and several studies have focused on constraining the timing and extent of the Last Glacial Maximum (LGM, ca. 20 ka) and post-LGM glacier fluctuations (Delunel et al., 2010; Le Roy et al., 2017). In this context, we select three small (6 - 15 km² area) catchments to cover the entire Vénéon valley, from the river source, at the heart of the Ecrins massif, to the confluence with the Romanche river where tributary glaciers had a lower morphological impact (Fig. 1B). The Pilatte catchment, the highest and most glaciated catchment, peaks at ~3600 m above sea level (a.s.l.), with valley bottoms around 2000 m. Modern glaciers represent ~14% of the catchment area (total catchment area of approximately 15 km²). With a downstream direction toward the north, its western and eastern parts are made of granitic or migmatic rocks (gneiss), respectively (source: French Geological Survey BRGM). The Etages catchment, partially-glaciated at present-day (~12 %), displays similar characteristics with an area of ~14 km² and an elevation range from 3564 to 1600 m a.s.l. at the confluence with the Vénéon river. The catchment is mainly underlaid by granites with crestlines composed of gneiss in its south-eastern part (Barféty et al., 1984; Delunel et al., 2014). Both catchments show steep hillslopes (>45-60°, Fig. 1C), located on the walls of the main U-shaped valley and along the highest rockwalls, considered as nunataks (Delunel et al., 2010; Marx et al., 2017), and a low-relief central valley bottom (Fig. 1D). The Etages catchment has been investigated by Delunel et al., 2014, with a detailed geomorphological mapping and use of quartz ¹⁰Be concentrations in detrital material to trace the potential geomorphic sources for river sediments. The third catchment, called "La Pisse", is completely unglaciated today and is smaller than the two other catchments (~6 km² total area). Its highest elevation at ~3050 m occurs at its southern crest, while its lowest elevation ~1250 m is at the confluence with the adjacent Villard catchment. Its lithology is dominated by granites even if the southwestern crest shows few Jurassic limestone outcrops. Slopes are mostly gentle in the upper part of the catchment and get steeper downstream along the valley rockwalls. Despite different glacial imprints and elevation, the slope distribution for the studied catchments is relatively similar (Fig. 1C), with a modal slope around 35° (0.7 m/m) for all three catchments.

179 180 181

182

These 3 investigated catchments have experienced a gradual post-LGM deglaciation, following the progressive glacier retreat along the Vénéon valley from downstream (Pisse catchment) to upstream





(Pilatte catchment). Following Delunel (2010), the Pisse catchment has likely started its deglaciation around 15 ka, while the Etage catchment may have been deglaciated between 13 and 7 ka. The glacier retreat in the Pilatte catchment has probably started slightly after the Etage catchment and can be considered at the end of the post-LGM deglaciation. As a consequence, the observed delay in glacier retreat between the three catchments (Fig. 1A) has likely been associated with a time-transgressive activation of periglacial processes like landslides, resulting in different topographic configurations today.

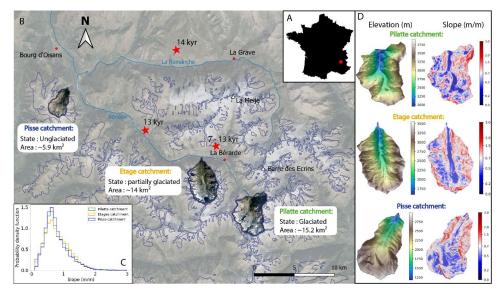


Figure 1: Geomorphological context of the study area. A) Location of the Ecrins massif (red dot) in France. B) Google satellite image of the Ecrins massif (background) with the three studied catchments and their characteristics: Pilatte (green label), Etages (yellow label) and Pisse (blue label). Blue thin line indicates the contour of the LGM ice extent (Delunel, 2010). Red stars report the estimated deglaciation timing (Delunel, 2010). C) Probability density function of topographic slope for the three studied catchments (25-m resolution DEM from the French National Geographic Institute IGN). Similar distributions are observed, with a main slope mode around 0.7 m/m. D) Modern elevation and slope maps for the three studied catchments.

2.2 Characteristics of glacial-catchment profiles

To visualize the hillslope morphologies in our studied catchments, we made topographic transects (Fig.2) along the main valley. In the literature or on the field, classical glacial topographic features, including typical U-shape valleys (Fig. 3), are well documented, easily observable and have been suggested to result from the bimodal distribution of glacial erosion with elevation (e.g. Anderson et al., 2006; Egholm et al., 2009; Herman et al., 2011; Steer et al., 2012). The observed bimodal hypsometry of glacial landscapes (Brocklehurst & Whipple, 2006) defines the boundaries between the valley overdeepening, driven by fast-moving ice with intense abrasion and quarrying, and areas with slower-moving ice exerting less erosive power (Coutterand, 2010; Leith et al., 2014). Alternatively, this bimodal hypsometry may be attributed to different patterns of cold-climate erosion around the ELA (Liebl et al.,

https://doi.org/10.5194/egusphere-2025-2088 Preprint. Discussion started: 26 May 2025 © Author(s) 2025. CC BY 4.0 License.





210 2021). In both interpretations, the hillslope shoulder – a slope inflection between two steep hillslopes, 211 known as "shouldering" - is shaped during glacial periods (Louis, 1952; Valla, 2021). This topographic 212 shouldering would result in a bimodal distribution of catchment elevations with steep slopes associated to both the glacier valley flanks (low elevations) and to the nunataks-crestlines area (i.e. periglacial 213 214 regions at high elevations) (Coutterand, 2010; Liebl et al., 2021). 215 In our studied catchments, the two upper catchments (Pilatte and Etages catchments) highlight the U-216 shaped valley on each transect, even in the upstream part of the catchment. A slope inflexion is also 217 visible along most of the transect, which we refer to as "shouldering" (Fig. 3). For most of the transects, 218 the increase in slope furthest upstream corresponds to the glacial trimline (Penck, 1905). It corresponds 219 to the highest zone of the glacier extent and usually the limit between prevailing glacier erosion 220 processes and periglacial processes, as their elevations match with the upper limits of the glacier cirque 221 (Rootes & Clark, 2020) (Fig. 2). Conversely, the topographic transects for the unglaciated catchment 222 (Pisse) tend to reveal a V+-shape valley, especially in the lower part of the catchment. The upper profile, 223 however, is closer to those of the glacial and intermediate catchment, showing a clear inheritance from 224 previous glaciations. 225 In the following, we will name the three studied catchments according to their glacial morphology 226 imprint, i.e 'glacial', 'intermediate glacial-fluvial' and 'fluvial' for the Pilatte, Etages and Pisse 227 catchments, respectively. 228



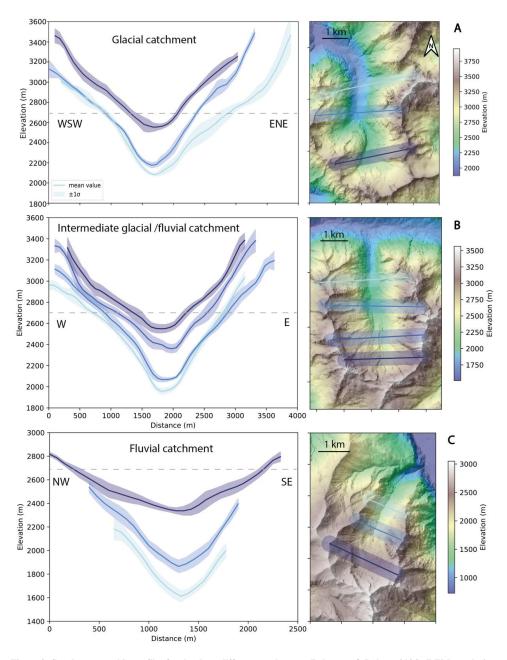


Figure 2: Swath topographic profiles for the three different catchments (Lehmann & Robert, 2024) (DEM, resolution: 50 cm, ESPG2154, from the French National Geographic Institute, Cusicanqui, 2024): (A) Glaciated catchment (Pilatte), (B) intermediate glacial-fluvial catchment (Etages), and (C) fluvial catchment (Pisse). Profiles are aligned based on their lowest area. The grey dot line illustrates the 2700 m elevation, a threshold elevation where the predicted landslides activity is lower (Figs. 6 & 7).





3. Modeling framework

Hylands is a reduced-complexity and stochastic landslide model (Campforts et al., 2020, 2022). It simulates both the erosion associated with deep-seated gravitational landslides and the induced sediment transport and deposition resulting from landslide runout. Hylands is part of the Landlab open-source framework (Barnhart et al., 2020; Hobley et al., 2017), which offers tools to combine multiple geomorphic laws on 2D regular grids, potentially applied to either synthetic topographies or digital elevation models (DEMs). In the following, we use the 25-m resolution DEMs from the BD ALTI of IGN (French National Geographic Institut), as initial model topographies for the three studied catchments. The catchment boundaries were obtained from the geo-processing tools ("Eau France" service website: https://reseau.eaufrance.fr/geotraitements/viewer/bassin-versant). We first here present the model and then our strategy for model calibration.

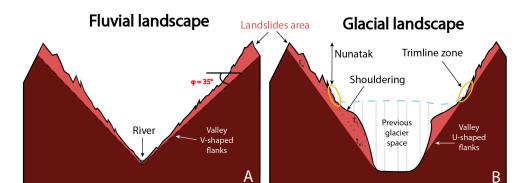


Figure 3: Conceptual sketches of theoretical topographic fluvial (A) and glacial (C) landscapes. A) Typical landscape dominated by fluvial erosion processes with V-shaped valley and homogeneous hillslopes slightly above the internal angle of friction ($\phi=35^\circ$ in this example). B) Landscape dominated by glacial erosion processes. The main morphological characteristics such as U-shaped valley, periglacial nunatak zone, shouldering or the trimline zone (yellow circle) are shown (modified from Louis, 1952; Coutterand, 2010). The light-red color indicates potential landscape areas affected by landslide activity.

3.1 The HyLands model

256 3.1.1 Landslide triggering

In HyLands, the landslide source model combines a spatial probability P_s and a temporal probability P_t to compute a landslide failure probability $P_{failure} = P_s * P_t$. The spatial probability is computed following a modified Culmann criterion (Campforts et al., 2020; Culmann, 1875), which is a Mohr-Coulomb criterion applied to a finite slope analysis:

$$P_S = \frac{H_S}{H_C}$$
, with $H_C = \frac{4C}{\rho g} \frac{\sin \beta \cos \varphi}{1 - \cos(\beta - \varphi)}$, (1)

where H_s (m) is the local hillslope height calculated between two adjacent cells of the grid and H_c is the maximum stable hillslope height (m), which depends on the cohesion C (kg.m⁻¹.s⁻²), ρ the rock density





set to 2700 kg.m⁻³, g = 9.81 m.s⁻² the gravitational acceleration, β the local topographic angle, and φ the

angle of internal friction (Eq. 1). Both C and φ are parameters that need to be calibrated in our modelling

267 approach.

However, HyLands is not a deterministic model as it combines this spatial probability of failure to a

temporal probability. Indeed, P_t controls the temporal occurrence of landslides and follows a Poisson

270 law (Campforts et al., 2022):

$$P_t = 1 - e^{-t/t_{LS}}, (2)$$

272

where t (yr) is the model time and t_{LS} (yr) is the return time of landslides triggering events. In turn, the

274 probability of failure of a given cell increases with time, until $P_{failure}$ becomes greater or equal to one,

leading to landslide triggering. The simulation time step is set to dt = 10 yr.

276 277

3.1.2 Landslide erosion and deposition

When a landslide event is triggered, the erosion scar generates a failure plan which initiates at the

279 triggering point. Following the Culmann criterion, the dip angle of this plan θ , is the bisector of the

local topography angle β , and the angle of internal friction of the material φ :

$$\theta = \frac{\beta + \varphi}{2} \tag{3}$$

282 The failure plane is propagated upstream of the critical node if the elevation of the neighboring cells

283 exceeds the rupture surface. In this case, all the DEM cells above this surface are considered as unstable

and mobilized by landsliding.

285 Landslide-derived sediments can either be transported as wash load, determined by the fraction of fines,

286 Ff in the model, or redistributed using a non-local nonlinear deposition scheme (Campforts et al., 2022).

287 Because our first goal is to study landslide erosion without any potential feedback of deposited

sediments, we set the fraction of fine sediments Ff to 1, meaning that all sediments are instantaneously

evacuated. It also means that in our set-up no topographic change can occur below the triggering points

290 of simulated landslide sources.

291292

293

294

295

296

297298

299

300

3.2 Strategy for model calibration

Our objective is to use a calibrated and physically sound landscape evolution model, based on HyLands, to predict landslide activity during postglacial conditions in our study area. Note that in these simulations, we only consider the role of landslides in landscape evolution and erosion dynamics, without modeling fluvial erosion nor tectonic activity (e.g., uplift rate). We also assume that gravitationally triggered landslides as simulated in HyLands, represent the combination of mass wasting events in alpine topography including rockfalls, debris flows, and shallow to deep-seated landslides, capturing the diverse range of slope failure processes. Our model calibration is performed on the Etages catchment following two steps:

https://doi.org/10.5194/egusphere-2025-2088 Preprint. Discussion started: 26 May 2025 © Author(s) 2025. CC BY 4.0 License.





301 1) Calibrating φ and C, which control the spatial probability of landslide occurrence, by comparing the
 302 modelled landslides area-frequency distribution (3.3.2) and size-volume scaling relationship (3.3.3),
 303 with the ones of natural landslide datasets (Fig. 4; Delgado et al., 2022; Guzzetti et al., 2002).

with the ones of natural landslide datasets (Fig. 4; Delgado et al., 2022; Guzzetti et al., 2002). 2) Calibrating the landslide return time t_{LS} , which sets the temporal probability of landslide occurrence, by comparing modelled catchment-averaged erosion rates and observed erosion data derived from quartz ¹⁰Be concentrations in stream sediments (3.3.4, Fig. 5), ranging between 0.27 and 1.1 mm/yr in the Ecrins massif (Delunel et al., 2010). For the Vénéon valley and the studied catchments (i.e. Etages catchment), we can reduce the interval from 0.7 to 1.1 mm/yr for our model calibration (Fig. 5). Assuming that a rock sample records quartz ¹⁰Be accumulation over the time period corresponding to the upper 60 cm below the surface (Delunel et al., 2010; von Blanckenburg, 2005), ¹⁰Be-derived erosion rates record apparent integration times of around 500 to 2500 yr. We thus select a simulation time of 1500 yr for the model calibration phase.

Some combinations of parameters (φ , C, t_{LS}) lead to too few landslides, preventing a statistical analysis of their resulting size distribution. To overcome this issue, we generated a large amount of landslide events and selected a similar number of landslides per simulation. Then, we had to(1) compile multiple simulations with similar parameters but different stochastic occurrence (different seeds), (2) reduce the return time ($t_{LS} = 100$). Because t_{LS} controls the occurrence of landslides without impacting their geometry, a small value of t_{LS} induces simulation outputs with large landslide datasets. This is particularly true given that the potential for landsliding remain significant throughout the simulation. The first approach was used for all the parameter calibration (Figs. 4A-C, 5), while the second approach was only used in the landslide size-frequency calibration (Fig. 4A) because the modified return time value can induce changes in landslide volumes and occurrences, and thus in output catchment-averaged erosion rates (Fig. 5).

3.3 Model calibration

3.3.1 Calibration of the angle of internal friction: landslide area-frequency distribution

Because we are lacking detailed compilation of alpine mass-wasting events, HyLAnds will be calibrated against global compilations of landslide data. More specifically, we aim at constraining the cohesion and angle of internal friction parameters. Although not calibrated to our specific field site, this general calibration will allow assessing the impact of gravity driven erosion in high alpine terrain and therefore provides sufficient for this study. For our calibration runs, we run HyLands from existing topography of the three catchments and set model parameters not involved in the calibration equal to those as reported in Table S1.



338

339340

341 342

343 344

345

346 347

348

349

350

351

352

353

354 355

356

357 358



Field inventories of landslides and rockfalls show a well-known shape for the frequency distribution of landslide area, highlighting several characteristics of a power-law relationship (Delgado et al., 2022; Guzzetti et al., 2002; Jeandet et al., 2019; Malamud et al., 2004; Stark & Hovius, 2001; Tanyaş et al., 2019; Tebbens, 2020): (1) the rollover value, matching the highest frequency of the landslide-area distribution, (2) the power-law scaling exponent, α , defined from the slope of the linear regression measured for large landslides events and (3) the cutoff value, related to the divergence of the distribution from a power-law scaling. With the exception of few parameter combinations (in the range of tested parameters of friction and cohesion), the simulated landslides size-frequency distributions we obtained not display any clear rollover. This lack of rollover is probably due to the coarse resolution of the grid (25 m) which makes it impossible to visualize small landslides, we do not use this criterion for our model calibration approach. The power-law scaling exponent is a key parameter as it describes the frequency of intermediate to large landslides, which convey most of the eroded volume. This exponent also varies significatively with the internal angle of friction (Fig. 4B). As no power-law exponent value exists for the French Alps landslide-rockfall inventories, we use as a reference the mean value $\alpha_{mean} = -$ 2.3 suggested by (Van Den Eeckhaut et al., 2007) from a global landslide compilation. (Tanyaş et al., 2018, 2019) also carried out a landslide compilation and analysis of landslide size-frequency distributions, proposing a slightly higher power-law exponent ($\alpha_{mean} = -2.5$). However, this inventory only considers earthquake-induced landslides. In addition, power-law exponents tend to be smaller for igneous or metamorphic rock (such as present in our study area) (Bennett et al., 2012), so we retain the value of -2.3 for our model calibration. In our calibration phase, we set the cutoff area at 3. 10⁴ m² based on the shape of the linear regression fit and the good value of the Pearson correlation coefficient (Fig. 4A). Our cutoff value seems to be smaller but overall consistent with previously reported values (Tanyas et al., 2018; 2019).

359360361

362363

364

365366

367368

369

370

371

372

373

The simulated landslide size-frequency distribution (Fig. 4A), in a log-log plot, illustrates the decrease in landslide number when increasing landslide size. From all simulated landslides (5. 10^4 in total; see Section 3.2), we randomly select 20 000 landslides to construct the landslide size-frequency distribution. This method ensures a homogeneous number of events between different combinations of input parameters (Fig. 4B). Therefore, we compare the simulated power-law scaling exponent α , resulting from different combinations of cohesion (C) and internal friction angle (φ), with the literature power-law exponent of -2.3. The power-law regression is computed using a log-log linear fit. The output matrix (Fig. 4B) shows a gradient for the power-law exponent α with increasing φ values. In our simulations, α varies strongly, between -1.7 and -3.1, when changing the internal angle of friction (31-39°, Fig. 4B). This range is consistent with global compilations of power-law exponents for landslide-area scaling (Tanyaş et al., 2018, 2019; Van Den Eeckhaut et al., 2007). We also observe little variability in α with cohesion (C). Therefore, we fix the internal angle of friction at $\varphi = 35^{\circ}$ which leads to simulated values of α close to -2.3. As the cohesion parameter seems to not influence the power-law exponent of the





landslides size-frequency distribution, we calibrate this parameter using an alternative strategy (see section 3.3.3).

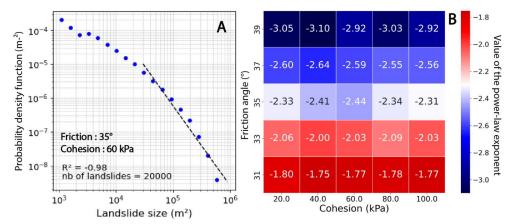


Figure 4: Calibration approach for the internal angle of friction and the cohesion in HyLand model. Calibration outcomes result from multiple simulations, with similar input parameters, to get a larger dataset of landslides (see text for discussion). A) Landslide size distribution, with a linear fit (dashed black line) on the power-law tail of the distribution. The cutoff value (i.e minimum size where the linear fit starts) is set to 3. 10^4 m². B) Calibration matrix between the internal angle of friction (ϕ) and the cohesion (C). The angle of friction is calibrated based on the minimum difference between the power-law exponent of the simulated size distribution and the reference value (-2.3; van den Eeckhaut et al., 2007). Blue colors indicate output power-law exponents smaller than the reference value (-2.3, white colors) and red colors indicate predicted power-law exponents higher than the reference value.

As a verification of our model calibration, we also simulate the area-volume relationship for simulated landslide distributions (Fig. S1). The relevant cloud of landslides events (n=426) shows a power-law scaling similar to those observed elsewhere with an intercept value of 0.84 and an exponent value γ =1.49 (Fig. S1) (Larsen et al, 2010; Wood et al, 2015).

3.3.3 Calibration of landslide return time and cohesion: 10 Be-derived erosion rate

To calibrate the cohesion and the landslide return time parameters, we compare simulated and 10 Bederived catchment-averaged erosion rates (3.2, Fig. 5). Both model parameters impact nonlinearly the output erosion rate, and increasing t_{LS} or C leads to lower output erosion rates (Fig. 5). Several combinations of parameters predict an output catchment-averaged erosion rated within the expected range (0.7 – 1.1 mm/yr): 1) a high C=100 kPa associated with a short t_{LS} =80 kyr, 2) a small C=40 kPa associated with a long t_{LS} =250 kyr, or 3) an intermediate parameter combination with C=60 kPa and t_{LS} =150 kyr. These three model parameterizations also lead to roughly similar spatial and temporal patterns in landslide activity. In the following, we therefore use the intermediate parameter combination (Fig. 5).





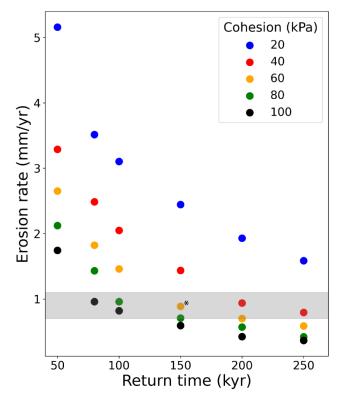


Figure 5: Calibration of the landslide return time and cohesion parameters based on the simulated catchment-averaged landslide erosion rate. Considering the calibrated angle of internal friction (35°, Fig. 4B), each dot represents a particular combination of landslide return time and cohesion (color code indicating the cohesion value). The selected combination is identified with a stars (*). The simulated erosion rate is an averaged catchment-scale erosion rate over a compilation of 20 different simulations (1500 yr duration). The grey band illustrates the range of literature values (0.7-1.1 mm/yr; Delunel et al., 2010).

4. Results

4.1 Spatial and temporal distribution of landslide activity

Using the calibrated model, we investigate the impact of landslide activity on catchment topographic changes over 100 kyr (timescales for glacial-interglacial cycles). Over this timescale, the calibrated landscape evolution model generates different spatial patterns of landslide erosion across the three studied catchments (Fig. 6). In each catchment, landslide erosion is distributed heterogeneously, ranging from areas experiencing an intense landslide activity and significant topographic changes to overall unaffected areas. For the Pilatte catchment (glacial), significant topographic changes, up to 500 m, occur along its northeast ridges. Elsewhere, predicted landslides lead to smaller topographic changes, around 100 m (Fig. 6A). The intermediate glacial-fluvial catchment (Etages) shows erosion patches along its crests and summit walls. In some areas, cumulated erosion reaches 350 m, while shallower landslides are observed on low-elevation hillslopes, just above the valley bottom (Fig. 6B). For the Pisse catchment (fluvial), landslide erosion is mainly focused on the downstream parts of the catchment where the valley narrows and slopes become steeper. Cumulated landslide erosion reaches up to 250 m, however, the

https://doi.org/10.5194/egusphere-2025-2088 Preprint. Discussion started: 26 May 2025 © Author(s) 2025. CC BY 4.0 License.

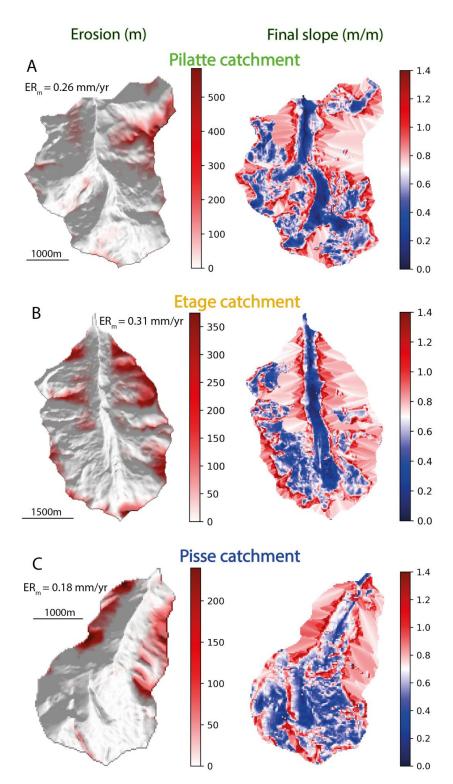




upper part of the catchment shows limited landslide activity (Fig. 6C). The final slopes across the three
 catchments clearly highlight the locus of landslide activity. Indeed, landsliding results in homogeneous
 slopes which only slightly exceeds the internal angle of friction (i.e., 0.7, represented by white color in
 Fig. 6).











431

432

433

Figure 6: Simulation results of cumulative landslide erosion and final slope distribution for the studied different catchments (A - Pilatte, B - Etages, C - Pisse). Left panels display landslide erosion patterns with cumulative landslide erosion (red color) over 100-kyr simulation duration on the modern hillshade DEM. Right panels show the final slope distributions where the landslide activity results in more homogenous slope patterns around the input internal angle of friction (0.7 m/m, white colors).

434 435

4.2 Spatial distribution of landslides 436 For each catchment, we investigate the simulated evolution of both the hypsometric and topographic 437 slope distributions (i.e. 2D histograms of catchment slope and elevation, Fig. 7A,D,E). As expected 438 from the modern slope distribution (Fig. 1C), the initial catchment topographies (i.e., at 0 kyr) show a 439 similar modal slope around 0.6 m/m. This modal slope is reached at different elevations for the different 440 441 catchments: 2800, 2600 and 2600 m a.s.l. for the glacial, intermediate glacial-fluvial and fluvial 442 catchment, respectively (Fig. 7A,D,G). The initial model topographies of the Pilatte (glacial) and Etage (intermediate glacial-fluvial) 443 catchments show a bimodal distribution of the elevations for steep slopes (Fig. 7A,D et 8) (Fig. S2). 444 The steepest slopes of the glacial catchment range between 2 and 4.5 m/m (i.e between ~63 and 77°) 445 and are mostly restricted to the highest elevations (3000- 4000 m) (Fig. 7A). A second peak of steep 446 447 slopes, with lower magnitudes $(1.5 - 2.5 \text{ m/m} \text{ i.e} \sim 56^{\circ} - 68^{\circ})$, is found around 2400 m. The intermediate glacial-fluvial catchment also shows an initial topography with two similar 'peaks' of steep slopes 448 frequency (Fig. 8C). We observe maximum slopes around 3 m/m (~70°) between 2700 and the 449 catchment crestline (~3500 m), and in a narrower elevation range from around 2000 to 2400 m (Fig. 450 7D). On the contrary, the fluvial catchment differs from the other catchments due to the relative 451 homogeneous distribution of slopes with elevation (Fig. 7G; Fig.S3). Throughout the simulations, 452 453 catchment slopes exceeding the friction angle at 0.7 m/m are affected by landslides, especially in the glacial catchment where significant changes can be noticed already after only 10 kyr simulation (Fig. 454 455 7B,E). Overall, after 100 kyr simulation, landslide activity has erased most of the steep slopes (almost three time less steep slopes, for high elevations, at the end of the simulation, Fig. 8C), i.e. above ~1.5 456 457 m/m, reducing significantly in turn the bimodal distribution of elevation for the steep slopes (Figs. 7C,F 458 & 8C). The maximum catchment elevation has decreased for the glacial and intermediate glacial-fluvial 459 catchments, while it remains approximately constant for the fluvial catchment after 100 kyr of 460 simulation. 461 During the simulations, we also observe a progressive increase in slope frequency slightly below 1 m/m (i.e, 45°), concentrated around 2600 - 3200 m, 2400 - 3000 m and 1900 - 2600 m for the glacial, 462 intermediate glacial-fluvial and fluvial catchments, respectively (Figs. 7C,F,I & 8B). This new slope 463 distribution evidences the shift from the initial steep slopes to final intermediate slopes that are closer 464 465 to the input internal friction.



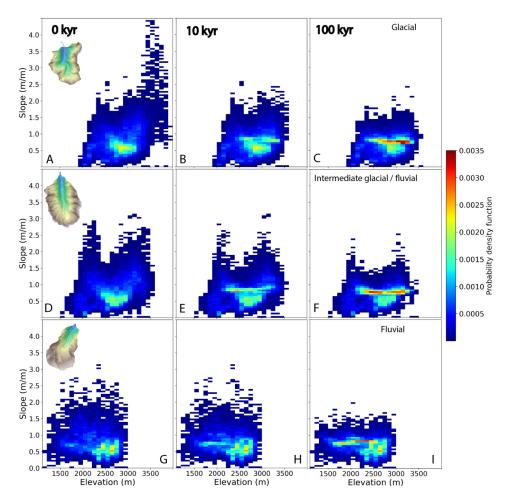


Figure 7: 2D histograms of the catchment slope distributions (color scale) with elevation. The temporal evolution of catchments slopes and elevations during simulations is monitored at three different time steps: 0, 10, an, 100 kyr (left, middle and right, respectively). Each row shows model results for a particular catchment: Pilatte (glaciated, A-B-C), Etages (intermediate glacial-fluvial, D-E-F), and Pisse (fluvial, G-H-I). For all three catchments, steep slopes are erased and catchment slopes tend toward more homogeneous slopes around the input internal angle of friction (0.7 m/m, i.e. 35°).



476

477

478 479

480

481 482

483

484

485

486 487

488

489

490 491

492

493 494

495

496 497



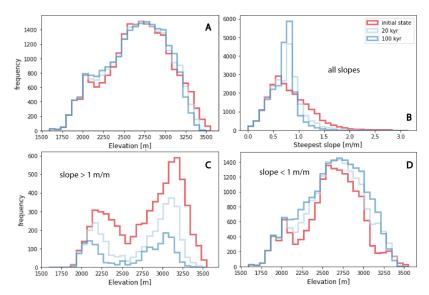


Figure 8: For the Etages catchment (intermediate glacial-fluvial), temporal evolution of (A) elevation distribution, (B) slope distribution, (B) Elevation distribution with slope threshold values (above or below 1m/m). The colors illustrate the initial topography (red), an intermediate stage $(20 \ kyr - light \ blue \ line)$ and the final topography $(100 \ kyr - dark \ blue)$.

4.3 Temporal distribution of landslides

We now investigate the relationship between topographic changes and landslide activity (Fig. 9). Here, we identify each landslide by its time of occurrence and its triggering location, corresponding to its lowest elevation (Fig. 9). First, our results highlight the bimodal elevation distribution of the simulated landslides, roughly above 2800 m and below 2400 m, which appears persistent with time for the glacial and intermediate glacial-fluvial catchments (Fig. 9A,B). These two catchments also show an intense landslide activity for the first 20 kyr of simulation, with an apparent progressive decay with time. Large landslides occur throughout the 100 kyr of simulation time, illustrating the stochastic nature of landslide occurrence in HyLands simulations. These observations are supported by the cumulative distribution of landslides volume through simulation time (Fig. 10A-C). For the glacial and intermediate glacial-fluvial catchments, more than half of the total landslide volume is predicted before 20 kyr. However, the cumulative number of landslides increases with time for these catchments. This discrepancy between the total landslide volume and the number of landslides may illustrate the preferential occurrence of large landslides within the first 20 kyr. This interpretation is supported by the change in the probability density function of the landslide volumes after 20 kyr simulation time (Fig S5). For these two (intermediate) glacial catchments, the difference in the exponent of the power-law scaling indicates the higher frequency of large landslides within the 20 kyr of simulation time (Fig 7G-H). We do not observe this pattern for the fluvial catchment (Fig S4 C, F), although the largest landslides are still predicted during the first 20 kyr of simulation time.





 Another interesting result is the inverse relationship between the predicted landslide volume and the number of landslides at different catchment elevations: at low elevations (<2700 m), landslides are less frequent but large landslides are overrepresented; whereas at high elevations (>2700 m), landslides are more frequent but large landslides are underrepresented. This assessment is particularly true for the Pilatte (glacial) and Etages (intermediate glacial-fluvial) catchments (Fig. 10A-B). For instance, the Pilatte catchment (Fig. 10A) displays twice more landslide occurrences at high elevations (>2700 m), with only a slightly larger eroded volume above than below 2700 m elevation.

Observations are significantly different for the fluvial catchment as the landslides are rather homogeneously distributed in the catchment (Fig. 9C). However, the high occurrences of landslides in the first 20 kyr are still noticeable (Fig. 10C) and large landslides tend to occur preferentially at low elevation (<2200 m).

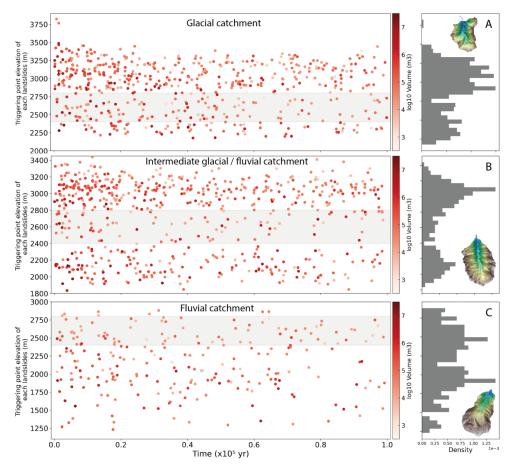


Figure 9: Triggering point elevation of each predicted landslide over the total simulation time ($100~\rm kyr$) and their associated volume (red gradient colors). The landslide distributions with elevation (right panels for distributions) appear bimodal for the glacial and intermediate catchments (A - B) with two main elevation ranges around 2100 and 3000 m and no clear altitudinal distribution of predicted landslides for the fluvial catchment (C).





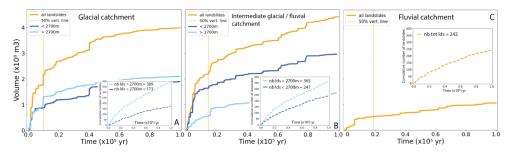


Figure 10: Cumulative distribution of the predicted landslide volumes over the total simulation time (100 kyr) for the glacial (Pilatte - A), intermediate glacial/fluvial (Etages - B) and fluvial (Pisse – C) catchments. The orange lines are the total cumulative landslide volumes, while the blue lines display the predicted cumulative volumes for landslides located above (light blue) and below (dark blue) an elevation threshold of 2700 m. The yellow vertical dashed lines indicate the simulation time when 50% of the total landslide volume is reached. Insets show the cumulative number of landslides generated during the simulation time for the two defined elevation classes.

4.4 Temporal evolution of landslide erosion rate

The term 'erosion rate' describes here only the predicted erosion induced by landslides and averaged over the catchment area. For each studied catchment, we compute the evolution of the catchment-averaged erosion rates using a 2-kyr time window, providing different statistics: mean, median, 25th and 75th percentiles of catchment-averaged erosion rates (Fig. 11). This temporal window emphasizes the general long-term trend of the predicted erosion rate by smoothing its high-frequency variations related to the stochasticity of landslide occurrence (Fig. S5). For all three catchments, the catchment-averaged erosion rates vary roughly between 10⁻⁵ and 10⁻¹ mm/yr when at least one landslide is triggered during the time window. The predicted mean erosion rate is always significantly higher than the median erosion rate (almost 10 times at the beginning of the simulation and around 100 times after 100 kyr of simulation time), but the progressive decreasing trend is observed for both two statistical measures. In addition, the 25th percentile rapidly becomes null, highlighting that the catchment-averaged erosion rate is driven by large but infrequent landslides.

The Pilatte (glacial) catchment (Fig. 11A) shows a particular high mean erosion rate, above 1 mm/yr, with a rapidly decreasing trend during the first 10 kyr. Then, the mean erosion rate decreases more slowly until 60 kyr and gets roughly constant at 0.1-0.2 mm/yr over the last 40 kyr of simulation. A similar trend is observed for the Etages (intermediate glacial-fluvial catchment, Fig. 11B), but the initial erosion rate is ~1 mm/yr and apparently lower than for the Pilatte (glacial) catchment. On the contrary, the Pisse (fluvial) catchment (Fig. 11C) shows a progressive decrease in the mean erosion rate, from ~0.6 to 0.06 mm/yr after 60 kyr of simulation, with no observed peak in erosion rate at the beginning of the simulation. The median value for the fluvial catchment reaches rapidly zero within the first 20 kyr of simulation, illustrating the lower frequency of landslide occurrence compared to the glacial and intermediate glacial-fluvial catchments. Overall and for all studied catchments, predicted landslide





erosion rates decrease by about an order of magnitude over 100 kyr, illustrating the progressive erasing of steep slopes associated to glacial morphological features.

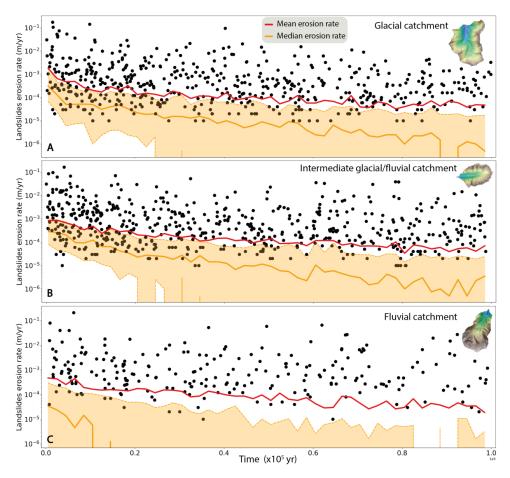


Figure 11: Temporal evolution of the landslide (catchment-averaged) erosion rate for the three studied catchments: A) Pilatte (glacial), B) Etages (intermediate glacial-fluvial). And C) Pisse (fluvial). Black dots illustrate the non-zero landslide erosion rates for each time step of one individual simulation, while red and orange lines depict respectively the mean and median (with 25th and 75th percentiles as dashed orange lines) erosion rates compiled from 20 individual simulations (with a smoothing temporal window of 2 kyr). For all catchments, the simulated landslide erosion rates decrease over time, especially during the first 20 kyr of simulation time, with different temporal trends depending on the catchment.

5. Discussion

5.1 Model limitations

Our landscape evolution model using HyLands has been designed to explore the hypothesis that landsliding represent a dominant geomorphological agent during postglacial periods. Our numerical simulations succeed in reproducing a pulse of landslides activity during the postglacial period and its





complex (non-homogeneous) impact on catchment hypsometry and slopes. However, this reduced-complexity model represents a simplified version of real hillslope dynamics, with limitations regarding its ability to predict in details all the richness of natural landforms, especially under the constraint of long simulation time (Tucker & Hancock, 2010). Therefore, we made several modeling choices (see Sections 3.2 and 3.3) to minimize potential feedback loops and interaction between erosion processes, which may have impacted our results as discussed below.

567568569

570

571572

573

574

575

576

577

578

579

580

581

582

583

584

585 586

587

588

589

590

591

592

593 594

595

596

562

563

564

565

566

5.1.1 Missing processes: uplift, fluvial erosion and transport

As mentioned earlier, the model does not account for the impact of uplift, which can be considered as a limitation. Given the present-day uplift rate in the western European Alps, around 1 mm/yr (Nocquet et al., 2016; Sternai et al., 2019), the total uplift over the simulation period (100 kyr) would be around 100 m. This theoretical uplift value is of the same order of magnitude than the average decrease in elevation caused by landslide erosion in the Etages (intermediate glacial-fluvial) and Pisse (fluvial) catchments (Figs. 6-7). In the Pilatte (glacial) catchment, the mean erosion is around 26 m, with maximum cumulated erosion of ~500 m. Therefore, integrating rock uplift in the model, from either geodynamics, tectonic activity or glacial isostatic rebound (Sternai et al., 2019), could counterbalance the overall decrease in catchment elevation observed in our results. Indeed, post-glacial rebound can occur at km scale, promoting local rock uplift and potentially considered to be a significant factor in triggering landslides in some regions (É. Cossart, 2013). In addition, rock uplift has also been proposed as modulating the post-glacial geomorphic response and landscape transition from glacial to fluvial states (Prasicek et al., 2015), rock uplift allowing faster relief turnover times. In addition to uplift, tectonic activity could be associated with seismicity, another well-known triggering factor for landslides (Keefer, 1984; McColl, 2012). However, our approach stays appropriate to assess the hillslope stability over 100 kyr, which is largely dependent on alpine topography, inherited from glacial-interglacial cycles, and mechanical strength. The impact of local earthquakes would mostly result in changing the timing of landslide activity, not the total volume of landslides. The catchment-averaged erosion rate of 1 mm/yr, derived from published cosmogenic nuclide data (Delunel et al., 2010) and used for the return time calibration, is integrating a large fluvial network with multiple erosion processes (fluvial, hillslope, landslide) at the scale of the Ecrins massif. Considering effective sediment connectivity in the catchment and only landsliding to derive our catchment erosion rate, 1 mm/yr is likely to be an end member minimum value for our simulations. Therefore, we ran a supplementary simulation with a lower cohesion value (20 kPa) while keeping the same return time (150 kyr), leading overall to a higher erosion rate (about 2-3 mm/yr, Fig. 5). The simulation results show a globally higher frequency of landslides, but with similar patterns in landslide occurrence, topographic changes and temporal trend in erosion rate (Fig.S6).





Finally, we did not include fluvial erosion and sediment export in our simulations. Ignoring sediment transport over a long timescale (100 kyr), integrating multiple glacial-interglacial periods, is a strong model limitation for alpine erosion dynamics (Schlunegger & Hinderer, 2003). Indeed, sediment transfer dynamics over the Quaternary period is associated with glacial dynamics (Antoniazza & Lane, 2021), coupling between hillslopes and channels (Hovius et al., 2000), fluvial incision (Leith et al., 2018; Valla et al., 2010) and potential transient sediment storage (Buechi et al., 2018). Rivers are also considered as the main agent of sediment transport during interglacial period (M. N. Koppes & Montgomery, 2009; Pitlick et al., 2021). Fluvial incision also leads to a lowering of the base level, which in turn creates more steep slopes at the hillslope foot. These changes participate to renew the landslide potential of these transient landforms. However, in this study we modeled a single interglacial period and provide a focus solely on hillslopes dynamics (i.e. no fluvial dynamics); both arguments result in a lower influence of the sediment dynamics for our results.

5.1.2 Model parametrization

Our modeling strategy and parameterization have inherent limitations, such as our initial input DEM (modern alpine topography) with a low resolution (25 m). Such resolution allows long simulation periods in a reasonable simulation time with the capability to still capture first-order erosion processes and topographic changes (Campforts et al., 2022). However, this relatively low resolution may hinder potential small-scale topographic roughness that could influence both landslide occurrence and magnitude. In addition, we ran our model simulations over 100 kyr, which is longer than any interglacial period during the Quaternary.

Another strong assumption is to ignore sediment deposition on the resulting simulated topography. Landslides are among th most efficient processes for producing sediments (Keefer, 1984) in mountainous areas, which can then be available for transport from hillslopes to the drainage network. The sediment connectivity (Cavalli et al., 2019), especially for bedload sediment, from hillslopes to channels is a key indicator to quantify sediment yields and morphological changes along the source-tosink profile (Comiti et al., 2019; Hooke, 2003; Lane et al., 2017; Micheletti et al., 2015). Thus, we explore the potential feedbacks of sediment deposition on landslide activity by testing the Hylands model with a null fine fraction parameter (Ff = 0), i.e. with a complete storage of landslide-produced sediment in the catchment. Coarse sediments are spread over the hillslopes, i.e. downstream of the landslide source, following a non-linear and non-local deposition law (Carretier et al., 2016). This deposition term depends on the transport distance which is driven by the critical slope, settled here equal to the tangent of the angle of internal friction (φ) (Campforts et al., 2022; Carretier et al., 2016). This new setup is the opposite of our main analysis (Ff = 1, Section 3.2), where we assumed a perfect sediment connectivity within the catchment, leading to instantaneous sediment export. Simulated sediment storage in the catchment (Ff = 0) causes a slight increase in landslide occurrence, especially at low elevations (<2700 m). We interpret this increase as a remobilization of the sediment deposits, which



634

635 636

637 638

639 640

641 642

643 644

645

646

647

648

649

650

662663

664

665

666

667



results in new landslide locations compared to previous simulations. The simulated deposition patterns are indeed mainly located in the valley bottom (Figs. S7-8). When the slopes of the deposits become greater than the internal angle of friction (0.7m/m, i.e. 35°), landslides can then occur. These landslides trigger in the sedimentary cover may also explain the slight landslides increase in the shouldering elevation zone (2400 – 2800 m, Figs. S7-8). However, the spatio-temporal landslide activity remains roughly similar to our previous simulations. Note that we have not computed the denudation rate without exported fine sediment because it would not be possible to compare it with measured value. Finally, our model parameterization assumes spatially uniform model parameters both within and between the three catchments. We used a single set of calibrated cohesion and internal angle of friction values (Figs. 3-4), without differentiation based on lithology, vegetation cover, elevation or glacial cover. This assumption may limit the model capacity in capturing the complex terrain roughness of alpine modern topographies, which may be a factor in increasing rock resistance to sliding in natural environments. For example, in our catchment, the effect of the tree cover at low elevations may not be apprehended by the model. Thus, the expected reduction in landslide occurrence due to root reinforcement or changes in soil moisture (Muñoz et al., 2016) is not simulated. In addition, the role of high-elevation permafrost, its spatial variability and temporal evolution, on landslide activity (Magnin et al., 2017), is not captured by our simulations.

5.2 The spatio-temporal landslide activity over the Quaternary period

651 The glacial inheritance of the alpine landforms, with glacial cirques, U-shaped and hanging valleys (Fig. 652 3), is still a current field of investigation in terms of their formation through multiple glacial cycles of 653 the Quaternary (Seguinot & Delaney, 2021) and their persistence during post-glacial periods (e.g. Herman & Braun, 2008; Prasicek et al., 2015). The relative contribution of glacial and fluvial erosion 654 to Quaternary relief evolution is still debated because of the difficulties to quantify erosion over glacial-655 interglacial timescales (Fox et al., 2015; Shuster et al., 2005; Sternai et al., 2013; Valla et al., 2011). 656 Moreover, some studies (M. N. Koppes & Montgomery, 2009; Leith et al., 2014, 2018; Montgomery & 657 658 Korup, 2011) have argued that Late-Pleistocene glaciations had only a limited impact on Alpine 659 topography, recent alpine relief evolution being then mainly driven by fluvial and hillslope processes 660 during interglacial. In this context, our numerical results bring some insights into the role of these 661 hillslope processes in the transition from glacial to fluvial morphologies.

5.2.1 Spatial landslide distribution and glacial imprint

The present-day catchment morphologies (Fig. 2) leave no doubt about the significant role of the glacial processes in shaping the investigated landscapes in the Ecrins massif (Fig. 1). However, our initial hypothesis about the capacity of landslides to erase this glacial topographic inheritance over the last post-glacial period is only partly validated by the simulation results.



669

670

671

672

673

674 675

676

677

678

679 680

681

682

683 684

685

686

687

688

689 690

691

692

693

694

695 696

697

698 699

700

701



First, the spatial landslide activity pattern (Fig. 9) reveals that the glacial morphologies are more subject to mass wasting processes. The steep slopes generated by glacial erosion along the U-shaped valley walls and at high elevation (crestlines and nunataks) produce a bimodal distribution of landslides with elevation, while the shouldering (Fig. 3), i.e., the gentler slope interval at mid-slope, induces a weak landslides activity. Therefore, our simulation results suggest that the transition from U-shaped to Vshaped valleys, as evidenced by the glacial (Pilatte) and fluvial (Pisse) catchments (Fig. 3) is highlighting the reshaping of the inherited glacial landscape through hillslope processes. However, the bimodal distribution of landslides with elevation is still noticeable after 100 kyr of simulation time (i.e., roughly ten times longer than the deglaciation period for the area). Moreover, the number of landslides and their spatial clustering is still significant for the glacial and intermediate glacial-fluvial catchments compared to the landslide pattern in the fluvial catchment (Pisse), which shows a more uniform distribution of landslides on hillslopes (Fig. 9). Thus, if the landslide activity and its spatial distribution can be considered as indicators of the hillslopes transition, our modeling results suggest that the glacial and intermediate glacial-fluvial catchments have not yet completed their post-glacial transition after 100 kyr simulation. Second, the landslide volume distributions also illustrate a specific dynamics of mass wasting events in formerly glaciated catchments. For the upper catchments (glacial and intermediate glacial-fluvial), our modeling results suggest that landslides are more frequent at higher elevations, near the crestlines, than at lower elevation near the valley bottoms (Fig. 10). This is consistent with the recent deglaciation of the upper catchments. Indeed, nunataks and crestlines in this interior part of the massif may still benefit from the stabilizing role of permafrost. Thus, the higher elevations of the catchment (i.e., above the trimline) still display steep and sharp slopes. Under a warming climate and the degradation of permafrost, these high-elevation and steep hillslopes will potentially be more and more prone to periglacial erosion processes (as it is already the case for the intermediate glacial-fluvial catchment). In parallel, our simulations predict large landslides at the lower elevations (Figs. 9 & 10). These results are consistent with the effect of debuttressing (i.e., stress variations resulting from glacial unloading) along the U-shaped valley wall following glacial recession (e.g. E. Cossart et al., 2008). This is also supported by the temporal clustering of the large landslides in the first 20 kyr. Yet, the occurrence of large landslides, due to their stochastic nature, remains occasional afterwards, which is consistent with other studies (Ivy-Ochs et al., 2017; Schwartz et al., 2017; Zerathe et al., 2014). Therefore, the persistence of landslide activity in the glacial and intermediate catchments, even after long simulation times, highlights that hillslope processes such as landslides, in response to glacial topographic inheritance, may not be the only factor explaining the fluvial morphology observed in our downstream catchment (Pisse).



704

705

706 707

708

709 710

711

712

713

714 715

716

717

718

719

720 721

722

723

724

725

726

727

728

729

730

731

732

733



5.2.2 Temporal landslide activity and transient topography

Here, we discuss our initial hypothesis, that all the studied catchments had the same glacial topographic imprint, and show that the three catchments have a distinct erosion dynamics explained by diachronous landslide activity following different glacial retreat times (Fig. 1). Following the previous spatial analysis (5.2.1), the observed temporal decrease in landslide occurrence and in predicted erosion rates over the first ~20 kyr (Fig. 11) reflects a decline in the proportion of unstable slopes during the postglacial period. The faster erosion modeled for the glacial and intermediate glacial-fluvial catchments, compared to the fluvial catchment, highlights the role of landsliding as a main geomorphological agent during the transition from glacial to inter-glacial conditions. This initial and gradual pulse of erosion, which differs between the studied catchments, reflects the distinct topographic states with respect to landslide susceptibility. The glacial catchment (Pilatte) has not experienced intense periglacial processes, such as landslides, for a sufficiently long period, resulting in this high erosion rate following debutressing of unstable glacial hillslopes (E. Cossart et al., 2008). The slowing down of erosion rates in the two upper catchments (glacial and intermediate glacial-fluvial) is also illustrating this long-term transitional stage, in which hillslope processes may continue to control sediment production, but at a smaller pace. With few landslides occurring at the end of our simulations, and associated to a low erosion rate, the Pisse (fluvial) catchment could be considered at the end of its transient phase and close to "postglacial topographic steady-state" dominated by hillslope processes (i.e no to few slope destabilizations). The modelled pulse of erosion for the postglacial phase implies that the Late Pleistocene period, marked by the transition from glacial to hillslope processes, has reactivated alpine landforms by reshaping new steep and unstable hillslopes along the U-shaped valleys or in the cirque areas. With its particular morphologies (Fig. 2), the glacial inheritance sustains the landslide erosion potential and may become an indicator of the glacial impact on alpine topographies. However, our model results also show that simulated landsliding over 100 kyr (duration exceeding the typical interglacial period) is not sufficient for the full transition from a glacial to a fluvial steady-state topography. Indeed, the simulated landslide activity - the bimodal landslide distribution (Fig. 9) - and the associated erosion rate are still significant at the end of our 100-kyr simulations, meaning that the hillslope system alone requires longer timescales than the typical Milankovitch cycle to reach a steady-state topography (i.e. a topography without hillslope instabilities). A longer simulation of 1 million years shows that a plateau is reached in the first 100kyr but that the erosion rate decreases gradually until 400 kyr (Fig. S9). At this time, the probability of failure is so small (probably because of no slope above the internal angle of friction), that the landslide-derived erosion rate is close to zero.

734735736

737

738

739

First, this observation can be compared to fluvial processes, which also have long timescales for reaching steady-state topographic conditions (Whipple, 2001). Since hillslope processes are also largely contributing to sediment production in alpine settings, the topographic response time to landsliding may play a role in the sediment cascade transfer which in turn would influence fluvial dynamics and erosion





740 rates. Second, this relatively long activity of the hillslope system during the interglacial period – 741 calibrated from cosmogenic-nuclide derived erosion rates (section 3.3.3) - is also consistent with the 742 absence of uplift and fluvial incision in our modeling approach. Including these model components in our simulations may decrease the duration of post-glacial landsliding activity for the studied catchments, 743 744 uplift promoting faster response of the hillslope-fluvial system as observed for natural settings (Prasicek 745 et al., 2015). Given the long persistence of landsliding from our simulations (>100 kyr), the observed differences in 746 747 landslide activity between the glacial/intermediate and fluvial catchments cannot be fully explained by 748 the time lag in glacier retreat and the duration of the interglacial period (~10 kyr, Fig. 1). We thus 749 propose that the glacial imprint may have been less intense in the fluvial (Pisse) catchment than in the 750 glacial and intermediate glacial-fluvial catchments (Pilatte and Etages). This confirms the non-uniform 751 impact of glacial processes on mountainous landforms (Herman et al., 2011; Sternai et al., 2013; van 752 der Beek & Bourbon, 2008), resulting from different ice extent/thickness and erosion efficiency over 753 glacial cycles (Pedersen & Egholm, 2013; Seguinot & Delaney, 2021).

754 755

5.3 Landsliding and topographic mountain evolution

756 5.3.1 The glacial/interglacial transition: a hot moment for alpine erosion

- 757 Glacial erosion also does not appear to be spatially-uniform throughout the glacial period (Seguinot &
- 758 Delaney, 2021), and field studies have shown increased glacial erosion during the deglaciation period
- 759 (M. N. Koppes & Montgomery, 2009). Therefore, hot moments of glacial dynamics occur at the end of
- the glacial period. Following this period, our model results suggest an additional pulse of rapid erosion,
- 761 associated to landsliding, at the onset of the interglacial period. Therefore, the glacial-interglacial
- 762 transition seems to concentrate the most rapid rates of erosion and in turn, may participate strongly to
- landscape changes and topographic relief evolution in alpine settings.
- However, our simulations were carried out on the current topography, which is already the results of 2
- 765 million years of successive glacial-interglacial cycles. Thus, the "hot-moment" of erosion that we
- 766 observe in the post-glacial period occurs in U-shaped valleys that are already well marked. As landslide
- 767 potential is maintained by steep slopes, this shape of mature glacial valley may increase landslides
- 768 activity compared with early Quaternary activity and increase in the same time the key role of hillslopes
- 769 processes in shaping long-term mountain topography (Burbank et al., 1996; Korup et al., 2007; Larsen
- 770 & Montgomery, 2012).

771 5.3.2 Toward a "landslide buzzsaw"?

- 772 The final landslide patterns from our simulations show interesting similarity with the morphological
- 773 changes associated with the glacial buzzsaw (Fig. 6). Previous studies have highlighted the impact of
- 774 glacial erosion on the mountain elevations and reliefs, referred as the 'glacial buzzsaw' (Egholm et al.,
- 775 2009; Herman et al., 2013, 2021; Mitchell & Montgomery, 2006; Thomson et al., 2010; Tomkin &





776 Braun, 2002). This theoretical concept, based on the observed correlation between the position of the 777 Equilibrium Line Altitude (ELA) and the mean and maximum height of mountains (Egholm et al., 2009), suggests that glaciers may have a strong control on mountain relief. In fact, by shaping cirques, glaciers 778 create steep slopes at high elevations (Brozović et al., 1997), increasing erosion above the ELA. 779 780 Although the "glacial buzzsaw" might be more complex in specific mountain ranges (Banerjee & Wani, 781 2018; Scherler, 2014), a concentration of surface area is usually observed around the ELA elevation 782 (Egholm et al., 2009, 2017; Liebl et al., 2021; Pedersen et al., 2010; Prasicek et al., 2020; Steer et al., 783 2012). 784 For the three studied catchments, most of the landslide scars occur close to the catchment boundaries, 785 i.e. along steep rock walls or on sharp ridges of the catchments. In addition, we observed a decrease in 786 the maximum catchment elevation and a concentration of hillslopes (around the angle of friction) at 787 specific elevations (Fig. 7). Thus, our simulations highlight that the topographic slopes above the ELA 788 seem strongly affected by landslide activity, appearing as a potential 'landslides buzzsaw' during 789 interglacial period. This concept may not be sustainable over long time periods since landslide activity 790 will limit the occurrence of steep hillslopes. However, over Quaternary glacial cycles, successive 791 glaciations and associated glacial/paraglacial erosion may sustain steep hillslopes at high elevations, 792 further promoting the "landslide buzzsaw" during subsequent interglacial periods as proposed for 793 instance for the European Alps (Delunel et al., 2020; Norton et al., 2010). This coupling between glacial 794 and hillslope processes would be reinforced by the topographic impact of landsliding, affecting steep 795 hillslopes at high elevations and producing larger low-relief areas at or above the ELA (Fig. 6). This 796 landscape conditioning would favor glacier development and erosion during the next glacial period, 797 maintaining or enhancing the potential for glacial buzzsaw (Pedersen & Egholm, 2013).

798 799

800

801

802

803

804

805

806 807

808

809

810 811

6. Conclusions

The successive glacial-interglacial transitions during the Quaternary period have promoted landscape disequilibrium between the inherited topography and the dominant geomorphological processes. The HyLands model was used to study how post-glacial landslides shape alpine landscapes. We focused on landslide rates, locations, and the influence of interglacial processes on long-term landscape evolution.

We modeled the topographic evolution of three distinct catchments located in the Ecrins massif (French Alps, Fig.1), that we identified as glacial, intermediate glacial-fluvial and fluvial catchments based on their morphological characteristics (Fig. 2). For these three catchments, the highest and steepest slopes are the first topographic areas impacted by landslides (Fig. 6). Topographic changes are particularly pronounced in the glacial and intermediate catchments, where we observed a bimodal distribution of landslides corresponding to the bimodal distribution of steep slopes generated by glacial erosion. In this case, the high and steep slopes are completely erased, inducing a decrease in slopes slightly greater than the internal angle of friction (Fig. 7, 8&9). This control of hillslope processes on the maximum mountain





812 elevations and the topographic reshaping at particular elevations leads us to propose similarities between 813 the 'glacial buzzsaw' concept and postglacial landslides activity. 814 The simulation results also highlight a high frequency of landslides during the first 20 kyr of our 815 simulations (Fig. 9&10), which is associated with higher erosion rates. Landslide activity and intensity, 816 and the resulting erosion rates, at the beginning of each simulation is following the morphological 817 gradient (from glacial to fluvial) observed in our three catchments (Fig.11). Therefore, glacial 818 topographic inheritance induces an intense post-glacial landslide activity, leading in turn possibly to 819 regular 'hot-moments' of landscape dynamics over the Quaternary. 820 Our study also concludes that hillslopes processes, such as landslides, alone cannot drive the transient 821 shift from glacial to fluvial morphology during the interglacial periods. The intensity of glacial erosion 822 and the extent of glacial advance may have been lower in downstream areas (i.e. in this study, within 823 the fluvial catchment), which may have led to a faster transition from glacial landscape to a fluvial one. 824 Finally, this study provides a basic but sound model for understanding landslide dynamics and their 825 impact on alpine landscape evolution. Additional components could be incorporated to enhance the 826 model, such as fluvial processes, permafrost degradation or non-uniform rock properties to better 827 capture the complex interactions occurring in mountain environment. In a future work, we intend to 828 model the interactions between hillslope processes and glacial processes over multiple glacial-829 interglacial cycles to better estimate their relative contributions. 830 831 Author contributions. CA conducted the model calibration and analysis with support from BC. CA, PS 832 and PV conceived the study and developed the methodology. All the authors were involved in writing 833 and reviewing the paper. 834 Competing interests. The contact author has declared that neither they nor their co-authors have any 835 competing interests. 836 Acknowledgements. The authors would like to thanks helpers who make this study easier, especially Diego Cusicanqui for the lidar extraction tool (https://doi.org/10.5281/zenodo.13832516) and Xavier 837 838 Robert for his help in adapting the simple-swath Python (https://doi.org/10.5281/zenodo.13771754). Thanks to Boris Gailleton for his advice on coding and to 839 840 Dimitri Lague for his insightful comments on landslide dynamics. 841 Financial support. This research has been supported by the H2020 European Research Council (grant 842 no. 803721). PGV acknowledges support from the French ANR-PIA programme (ANR-18-MPGA-843 0006). BC acknowledges support from the Dutch Research Council (NWO) under the grant 844 OCENW.M.23.027.





845	References
846	Anderson, R. S., Molnar, P., & Kessler, M. A. (2006). Features of glacial valley profiles simply
847	explained. Journal of Geophysical Research: Earth Surface, 111(F1).
848	https://doi.org/10.1029/2005JF000344
849	Antoniazza, G., & Lane, S. N. (2021). Sediment yield over glacial cycles: A conceptual model. <i>Progress</i>
850	in Physical Geography, 45(6), 842-865. https://doi.org/10.1177/0309133321997292
851	Ballantyne, C. K. (2002). Paraglacial geomorphology. <i>Quaternary Science Reviews</i> , 21(18), Article 18.
852	https://doi.org/10.1016/S0277-3791(02)00005-7
853	Banerjee, A., & Wani, B. A. (2018). Exponentially decreasing erosion rates protect the high-elevation
854	crests of the Himalaya. Earth and Planetary Science Letters, 497, 22-28.
855	https://doi.org/10.1016/j.epsl.2018.06.001
856	Barféty, J. C., Pécher, A., Bambrier, A., Demeulemeester, P., Fourneaux, J. C., Poulain, P. A., Vernet, J.,
857	& Vivier, G. (1984). Notice explicative de la feuille Saint-Christophe-en-Oisans à 1/50000.
858	Bureau de Recherches Géologiques et Minière: Orléans.
859	Barnhart, K. R., Hutton, E. W. H., Tucker, G. E., Gasparini, N. M., Istanbulluoglu, E., Hobley, D. E. J.,
860	Lyons, N. J., Mouchene, M., Nudurupati, S. S., Adams, J. M., & Bandaragoda, C. (2020). Short
861	communication: Landlab v2.0: a software package for Earth surface dynamics. Earth Surface
862	Dynamics, 8(2), 379-397. https://doi.org/10.5194/esurf-8-379-2020
863	Bennett, G. I., Molnar, P., Eisenbeiss, H., & McArdell, B. w. (2012). Erosional power in the Swiss Alps :
864	Characterization of slope failure in the Illgraben. Earth Surface Processes and Landforms,
865	37(15), 1627-1640. https://doi.org/10.1002/esp.3263
866	Blondeau, S., Gunnell, Y., & Jarman, D. (2021). Rock slope failure in the Western Alps : A first
867	comprehensive inventory and spatial analysis. Geomorphology, 380, 107622.
868	https://doi.org/10.1016/j.geomorph.2021.107622





869	Brardinoni, F., & Hassan, M. A. (2007). Glacially induced organization of channel-reach morphology in
870	mountain streams. Journal of Geophysical Research: Earth Surface, 112(F3).
871	https://doi.org/10.1029/2006JF000741
872	Brocklehurst, S. H., & Whipple, K. X. (2006). Assessing the relative efficiency of fluvial and glacial
873	erosion through simulation of fluvial landscapes. Geomorphology, 75(3), 283-299.
874	https://doi.org/10.1016/j.geomorph.2005.07.028
875	Broeckx, J., Rossi, M., Lijnen, K., Campforts, B., Poesen, J., & Vanmaercke, M. (2020). Landslide
876	mobilization rates: A global analysis and model. Earth-Science Reviews, 201, 102972.
877	https://doi.org/10.1016/j.earscirev.2019.102972
878	Brown, E. T., Stallard, R. F., Larsen, M. C., Raisbeck, G. M., & Yiou, F. (1995). Denudation rates
879	determined from the accumulation of in situ-produced 10Be in the luquillo experimental
880	forest, Puerto Rico. Earth and Planetary Science Letters, 129(1), 193-202.
881	https://doi.org/10.1016/0012-821X(94)00249-X
882	Brozović, N., Burbank, D. W., & Meigs, A. J. (1997). Climatic Limits on Landscape Development in the
883	Northwestern Himalaya. <i>Science</i> , <i>276</i> (5312), 571-574.
884	https://doi.org/10.1126/science.276.5312.571
885	Buechi, M. W., Graf, H. R., Haldimann, P., Lowick, S. E., & Anselmetti, F. S. (2018). Multiple
886	Quaternary erosion and infill cycles in overdeepened basins of the northern Alpine foreland.
887	Swiss Journal of Geosciences, 111(1), Article 1. https://doi.org/10.1007/s00015-017-0289-9
888	Burbank, D. W., Leland, J., Fielding, E., Anderson, R. S., Brozovic, N., Reid, M. R., & Duncan, C. (1996).
889	Bedrock incision, rock uplift and threshold hillslopes in the northwestern Himalayas. Nature,
890	379(6565), 505-510. https://doi.org/10.1038/379505a0
891	Campforts, B., Shobe, C. M., Overeem, I., & Tucker, G. E. (2022). The Art of Landslides: How
892	Stochastic Mass Wasting Shapes Topography and Influences Landscape Dynamics. Journal of
893	Geophysical Research: Earth Surface, 127(8), e2022JF006745.
894	https://doi.org/10.1029/2022JF006745





895	Campforts, B., Shobe, C. M., Steer, P., Vanmaercke, M., Lague, D., & Braun, J. (2020). HyLands 1.0 : A
896	hybrid landscape evolution model to simulate the impact of landslides and landslide-derived
897	sediment on landscape evolution. Geoscientific Model Development, 13(9), 3863-3886.
898	https://doi.org/10.5194/gmd-13-3863-2020
899	Carretier, S., Martinod, P., Reich, M., & Godderis, Y. (2016). Modelling sediment clasts transport
900	during landscape evolution. Earth Surface Dynamics, 4(1), 237-251.
901	https://doi.org/10.5194/esurf-4-237-2016
902	Carriere, A., Le Bouteiller, C., Tucker, G. E., Klotz, S., & Naaim, M. (2020). Impact of vegetation on
903	erosion: Insights from the calibration and test of a landscape evolution model in alpine
904	badland catchments. Earth Surface Processes and Landforms, 45(5), 1085-1099.
905	https://doi.org/10.1002/esp.4741
906	Cathala, M., Magnin, F., Ravanel, L., Dorren, L., Zuanon, N., Berger, F., Bourrier, F., & Deline, P.
907	(2024). Mapping release and propagation areas of permafrost-related rock slope failures in
908	the French Alps: A new methodological approach at regional scale. Geomorphology, 448,
909	109032. https://doi.org/10.1016/j.geomorph.2023.109032
910	Cavalli, M., Heckmann, T., & Marchi, L. (2019). Sediment Connectivity in Proglacial Areas. In T.
911	Heckmann & D. Morche (Éds.), Geomorphology of Proglacial Systems: Landform and
912	Sediment Dynamics in Recently Deglaciated Alpine Landscapes (p. 271-287). Springer
913	International Publishing. https://doi.org/10.1007/978-3-319-94184-4_16
914	Champagnac, JD., Valla, P. G., & Herman, F. (2014). Late-Cenozoic relief evolution under evolving
915	climate: A review. <i>Tectonophysics</i> , 614, 44-65. https://doi.org/10.1016/j.tecto.2013.11.037
916	Claessens, L., Schoorl, J. M., & Veldkamp, A. (2007). Modelling the location of shallow landslides and
917	their effects on landscape dynamics in large watersheds : An application for Northern New
918	Zealand. Geomorphology, 87(1), 16-27. https://doi.org/10.1016/j.geomorph.2006.06.039





919	Comiti, F., Mao, L., Penna, D., Dell'Agnese, A., Engel, M., Rathburn, S., & Cavalli, M. (2019). Glacier
920	melt runoff controls bedload transport in Alpine catchments. Earth and Planetary Science
921	Letters, 520, 77-86. https://doi.org/10.1016/j.epsl.2019.05.031
922	Cossart, É. (2013). Influence of local vs. Regional settings on glaciation patterns in the French Alps.
923	Geografia Fisica e Dinamica Quaternaria, 36(1), Article 1.
924	https://doi.org/10.4461/GFDQ.2013.36.3
925	Cossart, E., Braucher, R., Fort, M., Bourlès, D. L., & Carcaillet, J. (2008). Slope instability in relation to
926	glacial debuttressing in alpine areas (Upper Durance catchment, southeastern France):
927	Evidence from field data and 10Be cosmic ray exposure ages. Geomorphology, 95(1), 3-26.
928	https://doi.org/10.1016/j.geomorph.2006.12.022
929	Coutterand, S. (2010). Étude géomophologique des flux glaciaires dans les Alpes nord-occidentales au
930	Pléistocène récent. Du maximum de la dernière glaciation aux premières étapes de la
931	déglaciation [Phdthesis, Université de Savoie]. https://theses.hal.science/tel-00517790
932	Croissant, T., Lague, D., Steer, P., & Davy, P. (2017). Rapid post-seismic landslide evacuation boosted
933	by dynamic river width. Nature Geoscience, 10(9), Article 9.
934	https://doi.org/10.1038/ngeo3005
935	Culmann, K. (avec University of Michigan). (1875). Die graphische Statik. Zürich, Meyer & Zeller (A.
936	Reimann). http://archive.org/details/diegraphischest01culmgoog
937	Cusicanqui, D. (2024). cusicand/lidarhd_ign_downloader: V3.0 (Version v3.0) [Logiciel]. Zenodo.
938	https://doi.org/10.5281/zenodo.13832516
939	Dahlquist, M. P., West, A. J., & Li, G. (2018). Landslide-driven drainage divide migration. <i>Geology</i> ,
940	46(5), Article 5. https://doi.org/10.1130/G39916.1
941	Davy, P., Croissant, T., & Lague, D. (2017). A precipiton method to calculate river hydrodynamics,
942	with applications to flood prediction, landscape evolution models, and braiding instabilities.
943	Journal of Geophysical Research: Earth Surface, 122(8), 1491-1512.
944	https://doi.org/10.1002/2016JF004156





945	Delgado, F., Zerathe, S., Schwartz, S., Mathieux, B., & Benavente, C. (2022). Inventory of large
946	landslides along the Central Western Andes (ca. 15°–20° S) : Landslide distribution patterns
947	and insights on controlling factors. Journal of South American Earth Sciences, 116, 103824.
948	https://doi.org/10.1016/j.jsames.2022.103824
949	Delunel, R., Schlunegger, F., Valla, P. G., Dixon, J., Glotzbach, C., Hippe, K., Kober, F., Molliex, S.,
950	Norton, K. P., Salcher, B., Wittmann, H., Akçar, N., & Christl, M. (2020). Late-Pleistocene
951	catchment-wide denudation patterns across the European Alps. Earth-Science Reviews, 211,
952	103407. https://doi.org/10.1016/j.earscirev.2020.103407
953	Delunel, R., van der Beek, P. A., Bourlès, D. L., Carcaillet, J., & Schlunegger, F. (2014). Transient
954	sediment supply in a high-altitude Alpine environment evidenced through a 10Be budget of
955	the Etages catchment (French Western Alps). Earth Surface Processes and Landforms, 39(7),
956	890-899. https://doi.org/10.1002/esp.3494
957	Delunel, R., van der Beek, P. A., Carcaillet, J., Bourlès, D. L., & Valla, P. G. (2010). Frost-cracking
958	control on catchment denudation rates: Insights from in situ produced 10Be concentrations
959	in stream sediments (Ecrins–Pelvoux massif, French Western Alps). Earth and Planetary
960	Science Letters, 293(1), 72-83. https://doi.org/10.1016/j.epsl.2010.02.020
961	Densmore, A. L., Ellis, M. A., & Anderson, R. S. (1998). Landsliding and the evolution of normal-fault-
962	bounded mountains. Journal of Geophysical Research: Solid Earth, 103(B7), 15203-15219.
963	https://doi.org/10.1029/98JB00510
964	Dietrich, W. E., Reiss, R., Hsu, ML., & Montgomery, D. R. (1995). A process-based model for colluvial
965	soil depth and shallow landsliding using digital elevation data. Hydrological Processes, 9(3-4),
966	383-400. https://doi.org/10.1002/hyp.3360090311
967	Egholm, D. L., Jansen, J. D., Brædstrup, C. F., Pedersen, V. K., Andersen, J. L., Ugelvig, S. V., Larsen, N.
968	K., & Knudsen, M. F. (2017). Formation of plateau landscapes on glaciated continental
969	margins. Nature Geoscience, 10(8), 592-597. https://doi.org/10.1038/ngeo2980





970	Egholm, D. L., Nielsen, S. B., Pedersen, V. K., & Lesemann, JE. (2009). Glacial effects limiting
971	mountain height. Nature, 460(7257), 884-887. https://doi.org/10.1038/nature08263
972	Fox, M., Herman, F., Kissling, E., & Willett, S. D. (2015). Rapid exhumation in the Western Alps driven
973	by slab detachment and glacial erosion. Geology, 43(5), 379-382.
974	https://doi.org/10.1130/G36411.1
975	French, H. M. (2017). The Periglacial Environment. John Wiley & Sons.
976	Gallach, X., Carcaillet, J., Ravanel, L., Deline, P., Ogier, C., Rossi, M., Malet, E., & Garcia-Sellés, D.
977	(2020). Climatic and structural controls on Late-glacial and Holocene rockfall occurrence in
978	high-elevated rock walls of the Mont Blanc massif (Western Alps). Earth Surface Processes
979	and Landforms, 45(13), 3071-3091. https://doi.org/10.1002/esp.4952
980	Ganti, V., von Hagke, C., Scherler, D., Lamb, M. P., Fischer, W. W., & Avouac, JP. (2016). Time scale
981	bias in erosion rates of glaciated landscapes. Science Advances, 2(10), Article 10.
982	https://doi.org/10.1126/sciadv.1600204
983	George, D. L., & Iverson, R. M. (2014). A depth-averaged debris-flow model that includes the effects
984	of evolving dilatancy. II. Numerical predictions and experimental tests. Proceedings of the
985	Royal Society A: Mathematical, Physical and Engineering Sciences, 470(2170), 20130820.
986	https://doi.org/10.1098/rspa.2013.0820
987	Guzzetti, F., Malamud, B. D., Turcotte, D. L., & Reichenbach, P. (2002). Power-law correlations of
988	landslide areas in central Italy. Earth and Planetary Science Letters, 195(3), 169-183.
989	https://doi.org/10.1016/S0012-821X(01)00589-1
990	Hallet, B., Hunter, L., & Bogen, J. (1996). Rates of erosion and sediment evacuation by glaciers : A
991	review of field data and their implications. Global and Planetary Change, 12(1), Article 1.
992	https://doi.org/10.1016/0921-8181(95)00021-6
993	Heimsath, A. M., Furbish, D. J., & Dietrich, W. E. (2005). The illusion of diffusion: Field evidence for
994	depth-dependent sediment transport. Geology, 33(12), 949-952.
995	https://doi.org/10.1130/G21868.1





996	Hergarten, S., & Robl, J. (2015). Modelling rapid mass movements using the shallow water equations
997	in Cartesian coordinates. Natural Hazards and Earth System Sciences, 15(3), 671-685.
998	https://doi.org/10.5194/nhess-15-671-2015
999	Herman, F., Beaud, F., Champagnac, JD., Lemieux, JM., & Sternai, P. (2011). Glacial hydrology and
1000	erosion patterns: A mechanism for carving glacial valleys. Earth and Planetary Science
1001	Letters, 310(3), 498-508. https://doi.org/10.1016/j.epsl.2011.08.022
1002	Herman, F., & Braun, J. (2008). Evolution of the glacial landscape of the Southern Alps of New
1003	Zealand: Insights from a glacial erosion model. Journal of Geophysical Research: Earth
1004	Surface, 113(F2). https://doi.org/10.1029/2007JF000807
1005	Herman, F., & Champagnac, JD. (2016). Plio-Pleistocene increase of erosion rates in mountain belts
1006	in response to climate change. Terra Nova, 28(1), 2-10. https://doi.org/10.1111/ter.12186
1007	Herman, F., De Doncker, F., Delaney, I., Prasicek, G., & Koppes, M. (2021). The impact of glaciers on
1008	mountain erosion. Nature Reviews Earth & Environment, 2(6), 422-435.
1009	https://doi.org/10.1038/s43017-021-00165-9
1010	Herman, F., Seward, D., Valla, P. G., Carter, A., Kohn, B., Willett, S. D., & Ehlers, T. A. (2013).
1011	Worldwide acceleration of mountain erosion under a cooling climate. Nature, 504(7480),
1012	423-426. https://doi.org/10.1038/nature12877
1013	Hobley, D. E. J., Adams, J. M., Nudurupati, S. S., Hutton, E. W. H., Gasparini, N. M., Istanbulluoglu, E.,
1014	& Tucker, G. E. (2017). Creative computing with Landlab: An open-source toolkit for building,
1015	coupling, and exploring two-dimensional numerical models of Earth-surface dynamics. Earth
1016	Surface Dynamics, 5(1), 21-46. https://doi.org/10.5194/esurf-5-21-2017
1017	Hooke, J. (2003). Coarse sediment connectivity in river channel systems : A conceptual framework
1018	and methodology. Geomorphology, 56(1), Article 1. https://doi.org/10.1016/S0169-
1019	555X(03)00047-3





1020	Hovius, N., Stark, C. P., & Allen, P. A. (1997). Sediment flux from a mountain belt derived by landslide
1021	mapping. Geology, 25(3), 231-234. https://doi.org/10.1130/0091-
1022	7613(1997)025<0231:SFFAMB>2.3.CO;2
1023	Hovius, N., Stark, C. P., Hao-Tsu, C., & Jiun-Chuan, L. (2000). Supply and Removal of Sediment in a
1024	Landslide-Dominated Mountain Belt: Central Range, Taiwan. The Journal of Geology, 108(1),
1025	73-89. https://doi.org/10.1086/314387
1026	Ivy-Ochs, S., Martin, S., Campedel, P., Hippe, K., Alfimov, V., Vockenhuber, C., Andreotti, E., Carugati,
1027	G., Pasqual, D., Rigo, M., & Viganò, A. (2017). Geomorphology and age of the Marocche di
1028	Dro rock avalanches (Trentino, Italy). Quaternary Science Reviews, 169, 188-205.
1029	https://doi.org/10.1016/j.quascirev.2017.05.014
1030	Jeandet, L., Steer, P., Lague, D., & Davy, P. (2019). Coulomb Mechanics and Relief Constraints Explain
1031	Landslide Size Distribution—Jeandet—2019—Geophysical Research Letters—Wiley Online
1032	Library. https://agupubs.onlinelibrary.wiley.com/doi/full/10.1029/2019GL082351
1033	Keefer, D. K. (1984). Landslides caused by earthquakes. GSA Bulletin, 95(4), 406-421.
1034	https://doi.org/10.1130/0016-7606(1984)95<406:LCBE>2.0.CO;2
1035	Koppes, M., Hallet, B., Rignot, E., Mouginot, J., Wellner, J. S., & Boldt, K. (2015). Observed latitudinal
1036	variations in erosion as a function of glacier dynamics. <i>Nature</i> , 526(7571), 100-103.
1037	https://doi.org/10.1038/nature15385
1038	Koppes, M. N., & Montgomery, D. R. (2009). The relative efficacy of fluvial and glacial erosion over
1039	modern to orogenic timescales. Nature Geoscience, 2(9), 644-647.
1040	https://doi.org/10.1038/ngeo616
1041	Korup, O. (2006). Effects of large deep-seated landslides on hillslope morphology, western Southern
1042	Alps, New Zealand. Journal of Geophysical Research: Earth Surface, 111(F1), Article F1.
1043	https://doi.org/10.1029/2004JF000242





1044	Korup, O., Clague, J. J., Hermanns, R. L., Hewitt, K., Strom, A. L., & Weidinger, J. T. (2007). Giant
1045	landslides, topography, and erosion. Earth and Planetary Science Letters, 261(3), 578-589.
1046	https://doi.org/10.1016/j.epsl.2007.07.025
1047	Kuhlemann, J., Frisch, W., Székely, B., Dunkl, I., & Kázmér, M. (2002). Post-collisional sediment
1048	budget history of the Alps: Tectonic versus climatic control. International Journal of Earth
1049	Sciences, 91(5), 818-837. https://doi.org/10.1007/s00531-002-0266-y
1050	Lane, S. N., Bakker, M., Gabbud, C., Micheletti, N., & Saugy, JN. (2017). Sediment export, transient
1051	landscape response and catchment-scale connectivity following rapid climate warming and
1052	Alpine glacier recession. Geomorphology, 277, 210-227.
1053	https://doi.org/10.1016/j.geomorph.2016.02.015
1054	Langston, A. L., & Tucker, G. E. (2018). Developing and exploring a theory for the lateral erosion of
1055	bedrock channels for use in landscape evolution models. Earth Surface Dynamics, 6(1),
1056	Article 1. https://doi.org/10.5194/esurf-6-1-2018
1057	Larsen, I. J., & Montgomery, D. R. (2012). Landslide erosion coupled to tectonics and river incision.
1058	Nature Geoscience, 5(7), 468-473. https://doi.org/10.1038/ngeo1479
1059	Lavé, J., Guérin, C., Valla, P. G., Guillou, V., Rigaudier, T., Benedetti, L., France-Lanord, C., Gajurel, A.
1060	P., Morin, G., Dumoulin, J. P., Moreau, C., & Galy, V. (2023). Medieval demise of a Himalayan
1061	giant summit induced by mega-landslide. Nature, 619(7968), 94-101.
1062	https://doi.org/10.1038/s41586-023-06040-5
1063	Le Roy, M., Deline, P., Carcaillet, J., Schimmelpfennig, I., & Ermini, M. (2017). 10Be exposure dating of
1064	the timing of Neoglacial glacier advances in the Ecrins-Pelvoux massif, southern French Alps.
1065	Quaternary Science Reviews, 178, 118-138. https://doi.org/10.1016/j.quascirev.2017.10.010
1066	Lebrouc, V., Schwartz, S., Baillet, L., Jongmans, D., & Gamond, J. F. (2013). Modeling permafrost
1067	extension in a rock slope since the Last Glacial Maximum : Application to the large
1068	Séchilienne landslide (French Alps). Geomorphology, 198, 189-200.
1069	https://doi.org/10.1016/j.geomorph.2013.06.001





1070	Lehmann, B., & Robert, X. (2024). Simple_swath, a simple Python code to extract swath profile using
1071	a shapefile (Version 2.0.0) [Logiciel]. Zenodo. https://doi.org/10.5281/zenodo.13771754
1072	Leith, K., Fox, M., & Moore, J. R. (2018). Signatures of Late Pleistocene fluvial incision in an Alpine
1073	landscape. Earth and Planetary Science Letters, 483, 13-28.
1074	https://doi.org/10.1016/j.epsl.2017.11.050
1075	Leith, K., Moore, J. R., Amann, F., & Loew, S. (2014). Subglacial extensional fracture development and
1076	implications for Alpine Valley evolution. Journal of Geophysical Research: Earth Surface,
1077	119(1), 62-81. https://doi.org/10.1002/2012JF002691
1078	Liebl, M., Robl, J., Egholm, D. L., Prasicek, G., Stüwe, K., Gradwohl, G., & Hergarten, S. (2021).
1079	Topographic signatures of progressive glacial landscape transformation. Earth Surface
1080	Processes and Landforms, 46(10), 1964-1980. https://doi.org/10.1002/esp.5139
1081	Louis, H. (1952). Zur Theorie der Gletschererosion in Tälern. E&G Quaternary Science Journal, 2(1),
1082	12-24. https://doi.org/10.3285/eg.02.1.02
1083	Magnin, F., Josnin, JY., Ravanel, L., Pergaud, J., Pohl, B., & Deline, P. (2017). Modelling rock wall
1084	permafrost degradation in the Mont Blanc massif from the LIA to the end of the 21st century.
1085	The Cryosphere, 11(4), 1813-1834. https://doi.org/10.5194/tc-11-1813-2017
1086	Malamud, B. D., Turcotte, D. L., Guzzetti, F., & Reichenbach, P. (2004). Landslide inventories and their
1087	statistical properties. Earth Surface Processes and Landforms, 29(6), 687-711.
1088	https://doi.org/10.1002/esp.1064
1089	Martin, H. A., Peruzzetto, M., Viroulet, S., Mangeney, A., Lagrée, PY., Popinet, S., Maury, B.,
1090	Lefebvre-Lepot, A., Maday, Y., & Bouchut, F. (2023). Numerical simulations of granular dam
1091	break : Comparison between discrete element, Navier-Stokes, and thin-layer models.
1092	Physical Review E, 108(5), 054902. https://doi.org/10.1103/PhysRevE.108.054902
1093	Marx, H. E., Dentant, C., Renaud, J., Delunel, R., Tank, D. C., & Lavergne, S. (2017). Riders in the sky
1094	(islands): Using a mega-phylogenetic approach to understand plant species distribution and





1095	coexistence at the altitudinal limits of angiosperm plant life. Journal of Biogeography, 44(11),
1096	2618-2630. https://doi.org/10.1111/jbi.13073
1097	McColl, S. T. (2012). Paraglacial rock-slope stability. <i>Geomorphology</i> , 153-154, 1-16.
1098	https://doi.org/10.1016/j.geomorph.2012.02.015
1099	Métivier, F., Gaudemer, Y., Tapponnier, P., & Klein, M. (1999). Mass accumulation rates in Asia during
1100	the Cenozoic. Geophysical Journal International, 137(2), 280-318.
1101	https://doi.org/10.1046/j.1365-246X.1999.00802.x
1102	Meunier, P., Hovius, N., & Haines, J. A. (2008). Topographic site effects and the location of
1103	earthquake induced landslides. Earth and Planetary Science Letters, 275(3), 221-232.
1104	https://doi.org/10.1016/j.epsl.2008.07.020
1105	Micheletti, N., Lambiel, C., & Lane, S. N. (2015). Investigating decadal-scale geomorphic dynamics in
1106	an alpine mountain setting. Journal of Geophysical Research: Earth Surface, 120(10), Article
1107	10. https://doi.org/10.1002/2015JF003656
1108	Mitchell, S. G., & Montgomery, D. R. (2006). Influence of a glacial buzzsaw on the height and
1109	morphology of the Cascade Range in central Washington State, USA. Quaternary Research,
1110	65(1), 96-107. https://doi.org/10.1016/j.yqres.2005.08.018
1111	Montgomery, D. R., & Korup, O. (2011). Preservation of inner gorges through repeated Alpine
1112	glaciations. Nature Geoscience, 4(1), 62-67. https://doi.org/10.1038/ngeo1030
1113	Morriss, M. C., Lehmann, B., Campforts, B., Brencher, G., Rick, B., Anderson, L. S., Handwerger, A. L.,
1114	Overeem, I., & Moore, J. (2023). Alpine hillslope failure in the western US: Insights from the
1115	Chaos Canyon landslide, Rocky Mountain National Park, USA. Earth Surface Dynamics, 11(6),
1116	1251-1274. https://doi.org/10.5194/esurf-11-1251-2023
1117	Mudd, S. M., Harel, MA., Hurst, M. D., Grieve, S. W. D., & Marrero, S. M. (2016). The CAIRN
1118	method : Automated, reproducible calculation of catchment-averaged denudation rates from
1119	cosmogenic nuclide concentrations. Earth Surface Dynamics, 4(3), 655-674.
1120	https://doi.org/10.5194/esurf-4-655-2016





1121	Müller, T., Lane, S. N., & Schaefli, B. (2022). Towards a hydrogeomorphological understanding of
1122	proglacial catchments: An assessment of groundwater storage and release in an Alpine
1123	catchment. Hydrology and Earth System Sciences, 26(23), 6029-6054.
1124	https://doi.org/10.5194/hess-26-6029-2022
1125	Muñoz, E., Ochoa, A., & Cordão-Neto, M. (2016). Probabilistic assessment of precipitation-triggered
1126	landslides: The role of vegetation. E3S Web of Conferences, 9, 08001.
1127	https://doi.org/10.1051/e3sconf/20160908001
1128	Nocquet, JM., Sue, C., Walpersdorf, A., Tran, T., Lenôtre, N., Vernant, P., Cushing, M., Jouanne, F.,
1129	Masson, F., Baize, S., Chéry, J., & van der Beek, P. A. (2016). Present-day uplift of the western
1130	Alps. Scientific Reports, 6(1), Article 1. https://doi.org/10.1038/srep28404
1131	Norton, K. P., Abbühl, L. M., & Schlunegger, F. (2010). Glacial conditioning as an erosional driving
1132	force in the Central Alps. <i>Geology</i> , 38(7), 655-658. https://doi.org/10.1130/G31102.1
1133	Pedersen, V. K., & Egholm, D. L. (2013). Glaciations in response to climate variations preconditioned
1134	by evolving topography. <i>Nature</i> , 493(7431), 206-210. https://doi.org/10.1038/nature11786
1135	Pedersen, V. K., Egholm, D. L., & Nielsen, S. B. (2010). Alpine glacial topography and the rate of rock
1136	column uplift: A global perspective. Geomorphology, 122(1), 129-139.
1137	https://doi.org/10.1016/j.geomorph.2010.06.005
1138	Peizhen, Z., Molnar, P., & Downs, W. R. (2001). Increased sedimentation rates and grain sizes 2–4
1139	Myr ago due to the influence of climate change on erosion rates. Nature, 410(6831),
1140	891-897. https://doi.org/10.1038/35073504
1141	Penck, A. (1905). Glacial Features in the Surface of the Alps. <i>The Journal of Geology</i> , 13(1), 1-19.
1142	https://doi.org/10.1086/621202
1143	Perron, J. T. (2011). Numerical methods for nonlinear hillslope transport laws. <i>Journal of Geophysical</i>
1144	Research: Earth Surface, 116(F2). https://doi.org/10.1029/2010JF001801





1146	Production in French Alpine Rivers. Water Resources Research, 57(12), e2021WR030470.
1147	https://doi.org/10.1029/2021WR030470
1148	Portenga, E. W., & Bierman, P. R. (2011). Understanding earth's eroding surface with ¹⁰ Be. <i>College of</i>
1149	Arts and Sciences Faculty Publications. https://doi.org/10.1130/G111A.1
1150	Prasicek, G., Hergarten, S., Deal, E., Herman, F., & Robl, J. (2020). A glacial buzzsaw effect generated
1151	by efficient erosion of temperate glaciers in a steady state model. Earth and Planetary
1152	Science Letters, 543, 116350. https://doi.org/10.1016/j.epsl.2020.116350
1153	Prasicek, G., Larsen, I. J., & Montgomery, D. R. (2015). Tectonic control on the persistence of glacially
1154	sculpted topography. Nature Communications, 6(1), 8028.
1155	https://doi.org/10.1038/ncomms9028
1156	Ravanel, L., Magnin, F., & Deline, P. (2017). Impacts of the 2003 and 2015 summer heatwaves on
1157	permafrost-affected rock-walls in the Mont Blanc massif. Science of The Total Environment,
1158	609, 132-143. https://doi.org/10.1016/j.scitotenv.2017.07.055
1159	Roering, J. (2012). Landslides limit mountain relief. <i>Nature Geoscience</i> , 5(7), 446-447.
1160	https://doi.org/10.1038/ngeo1511
1161	Roering, J. J., Kirchner, J. W., & Dietrich, W. E. (1999). Evidence for nonlinear, diffusive sediment
1162	transport on hillslopes and implications for landscape morphology. Water Resources
1163	Research, 35(3), 853-870. https://doi.org/10.1029/1998WR900090
1164	Rootes, C. M., & Clark, C. D. (2020). Glacial trimlines to identify former ice margins and subglacial
1165	thermal boundaries: A review and classification scheme for trimline expression. Earth-
1166	Science Reviews, 210, 103355. https://doi.org/10.1016/j.earscirev.2020.103355
1167	Roussel, E., Marren, P. M., Cossart, E., Toumazet, JP., Chenet, M., Grancher, D., & Jomelli, V. (2018).
1168	Incision and aggradation in proglacial rivers: Post-Little Ice Age long-profile adjustments of
1169	Southern Iceland outwash plains. Land Degradation & Development, 29(10), 3753-3771.
1170	https://doi.org/10.1002/ldr.3127





Scherler, D. (2014). Climatic limits to headwall retreat in the Khumbu Himalaya, eastern Nepal.
Geology, 42(11), 1019-1022. https://doi.org/10.1130/G35975.1
Schlunegger, F., & Hinderer, M. (2003). Pleistocene/Holocene climate change, re-establishment of
fluvial drainage network and increase in relief in the Swiss Alps. Terra Nova, 15(2), 88-95.
https://doi.org/10.1046/j.1365-3121.2003.00469.x
Schwartz, S., Zerathe, S., Jongmans, D., Baillet, L., Carcaillet, J., Audin, L., Dumont, T., Bourlès, D.,
Braucher, R., & Lebrouc, V. (2017). Cosmic ray exposure dating on the large landslide of
Séchilienne (Western Alps): A synthesis to constrain slope evolution. Geomorphology, 278,
329-344. https://doi.org/10.1016/j.geomorph.2016.11.014
Seguinot, J., & Delaney, I. (2021). Last-glacial-cycle glacier erosion potential in the Alps. <i>Earth Surface</i>
Dynamics, 9(4), 923-935. https://doi.org/10.5194/esurf-9-923-2021
Shuster, D. L., Ehlers, T. A., Rusmoren, M. E., & Farley, K. A. (2005). Rapid Glacial Erosion at 1.8 Ma
Revealed by 4He/3He Thermochronometry. Science, 310(5754), 1668-1670.
https://doi.org/10.1126/science.1118519
Solomina, O. N., Bradley, R. S., Hodgson, D. A., Ivy-Ochs, S., Jomelli, V., Mackintosh, A. N., Nesje, A.,
Owen, L. A., Wanner, H., Wiles, G. C., & Young, N. E. (2015). Holocene glacier fluctuations.
Quaternary Science Reviews, 111, 9-34. https://doi.org/10.1016/j.quascirev.2014.11.018
Stark, C. P., & Hovius, N. (2001). The characterization of landslide size distributions. <i>Geophysical</i>
Research Letters, 28(6), 1091-1094. https://doi.org/10.1029/2000GL008527
Steer, P., Huismans, R. S., Valla, P. G., Gac, S., & Herman, F. (2012). Bimodal Plio–Quaternary glacial
erosion of fjords and low-relief surfaces in Scandinavia. <i>Nature Geoscience</i> , 5(9), Article 9.
https://doi.org/10.1038/ngeo1549
Sternai, P., Herman, F., Valla, P. G., & Champagnac, JD. (2013). Spatial and temporal variations of
glacial erosion in the Rhône valley (Swiss Alps): Insights from numerical modeling. Earth and
Planetary Science Letters, 368, 119-131. https://doi.org/10.1016/j.epsl.2013.02.039





Sternai, P., Sue, C., Husson, L., Serpelloni, E., Becker, T. W., Willett, S. D., Faccenna, C., Di Giulio, A.,
Spada, G., Jolivet, L., Valla, P., Petit, C., Nocquet, JM., Walpersdorf, A., & Castelltort, S.
(2019). Present-day uplift of the European Alps : Evaluating mechanisms and models of their
relative contributions. Earth-Science Reviews, 190, 589-604.
https://doi.org/10.1016/j.earscirev.2019.01.005
Stoffel, M., Trappmann, D. G., Coullie, M. I., Ballesteros Cánovas, J. A., & Corona, C. (2024). Rockfall
from an increasingly unstable mountain slope driven by climate warming. Nature Geoscience,
1-6. https://doi.org/10.1038/s41561-024-01390-9
Tanyaş, H., Allstadt, K. E., & van Westen, C. J. (2018). An updated method for estimating landslide-
event magnitude. Earth Surface Processes and Landforms, 43(9), 1836-1847.
https://doi.org/10.1002/esp.4359
Tanyaş, H., van Westen, C. J., Allstadt, K. E., & Jibson, R. W. (2019). Factors controlling landslide
frequency—area distributions. Earth Surface Processes and Landforms, 44(4), 900-917.
https://doi.org/10.1002/esp.4543
Tebbens, S. F. (2020). Landslide Scaling: A Review—Tebbens—2020—Earth and Space Science—
Wiley Online Library.
https://agupubs.onlinelibrary.wiley.com/doi/full/10.1029/2019EA000662
Thomson, S. N., Brandon, M. T., Tomkin, J. H., Reiners, P. W., Vásquez, C., & Wilson, N. J. (2010).
Glaciation as a destructive and constructive control on mountain building. <i>Nature</i> , 467(7313),
313-317. https://doi.org/10.1038/nature09365
Tomkin, J. H., & Braun, J. (2002). The influence of alpine glaciation on the relief of tectonically active
mountain belts. American Journal of Science, 302(3), 169-190.
https://doi.org/10.2475/ajs.302.3.169
Tucker, G. E., & Hancock, G. R. (2010). Modelling landscape evolution. Earth Surface Processes and





Valla, P. G., Shuster, D. L., & van der Beek, P. A. (2011). Significant increase in relief of the Europe Alps during mid-Pleistocene glaciations. <i>Nature Geoscience</i> , 4(10), 688-692. https://doi.org/10.1038/ngeo1242 Valla, P. G., van der Beek, P. A., & Lague, D. (2010). Fluvial incision into bedrock: Insights from morphometric analysis and numerical modeling of gorges incising glacial hanging valleys (Western Alps, France). <i>Journal of Geophysical Research: Earth Surface</i> , 115(F2). https://doi.org/10.1029/2008JF001079 Van Den Eeckhaut, M., Poesen, J., Govers, G., Verstraeten, G., & Demoulin, A. (2007). Characteri of the size distribution of recent and historical landslides in a populated hilly region. <i>Earth and Planetary Science Letters</i> , 256(3), 588-603. https://doi.org/10.1016/j.epsl.2007.01.01 van der Beek, P., & Bourbon, P. (2008). A quantification of the glacial imprint on relief developm in the French western Alps. <i>Geomorphology</i> , 97(1), Article 1. https://doi.org/10.1016/j.geomorph.2007.02.038 von Blanckenburg, F. (2005). The control mechanisms of erosion and weathering at basin scale for cosmogenic nuclides in river sediment. <i>Earth and Planetary Science Letters</i> , 237(3), 462-1238 Whipple, K. X. (2001). Fluvial Landscape Response Time: How Plausible Is Steady-State Denudated.	on der Beek, P. A. (2011). Significant increase in relief of the European ocene glaciations. <i>Nature Geoscience</i> , <i>4</i> (10), 688-692. 8/ngeo1242 , & Lague, D. (2010). Fluvial incision into bedrock: Insights from and numerical modeling of gorges incising glacial hanging valleys
Alps during mid-Pleistocene glaciations. <i>Nature Geoscience</i> , <i>4</i> (10), 688-692. https://doi.org/10.1038/ngeo1242 Valla, P. G., van der Beek, P. A., & Lague, D. (2010). Fluvial incision into bedrock: Insights from morphometric analysis and numerical modeling of gorges incising glacial hanging valleys (Western Alps, France). <i>Journal of Geophysical Research: Earth Surface</i> , <i>115</i> (F2). https://doi.org/10.1029/2008JF001079 Van Den Eeckhaut, M., Poesen, J., Govers, G., Verstraeten, G., & Demoulin, A. (2007). Characteri of the size distribution of recent and historical landslides in a populated hilly region. <i>Eart and Planetary Science Letters</i> , <i>256</i> (3), 588-603. https://doi.org/10.1016/j.epsl.2007.01.013 van der Beek, P., & Bourbon, P. (2008). A quantification of the glacial imprint on relief developm in the French western Alps. <i>Geomorphology</i> , <i>97</i> (1), Article 1. https://doi.org/10.1016/j.geomorph.2007.02.038 von Blanckenburg, F. (2005). The control mechanisms of erosion and weathering at basin scale for cosmogenic nuclides in river sediment. <i>Earth and Planetary Science Letters</i> , <i>237</i> (3), 462-1238 https://doi.org/10.1016/j.epsl.2005.06.030	ocene glaciations. <i>Nature Geoscience</i> , <i>4</i> (10), 688-692. 8/ngeo1242 , & Lague, D. (2010). Fluvial incision into bedrock: Insights from and numerical modeling of gorges incising glacial hanging valleys
https://doi.org/10.1038/ngeo1242 Valla, P. G., van der Beek, P. A., & Lague, D. (2010). Fluvial incision into bedrock: Insights from morphometric analysis and numerical modeling of gorges incising glacial hanging valleys (Western Alps, France). <i>Journal of Geophysical Research: Earth Surface, 115</i> (F2). https://doi.org/10.1029/2008JF001079 Van Den Eeckhaut, M., Poesen, J., Govers, G., Verstraeten, G., & Demoulin, A. (2007). Characteri of the size distribution of recent and historical landslides in a populated hilly region. <i>Eart and Planetary Science Letters, 256</i> (3), 588-603. https://doi.org/10.1016/j.epsl.2007.01.01233 van der Beek, P., & Bourbon, P. (2008). A quantification of the glacial imprint on relief developmed in the French western Alps. <i>Geomorphology, 97</i> (1), Article 1. https://doi.org/10.1016/j.geomorph.2007.02.038 von Blanckenburg, F. (2005). The control mechanisms of erosion and weathering at basin scale for cosmogenic nuclides in river sediment. <i>Earth and Planetary Science Letters, 237</i> (3), 462-1238 https://doi.org/10.1016/j.epsl.2005.06.030	8/ngeo1242 , & Lague, D. (2010). Fluvial incision into bedrock: Insights from and numerical modeling of gorges incising glacial hanging valleys
Valla, P. G., van der Beek, P. A., & Lague, D. (2010). Fluvial incision into bedrock: Insights from morphometric analysis and numerical modeling of gorges incising glacial hanging valleys (Western Alps, France). <i>Journal of Geophysical Research: Earth Surface, 115</i> (F2). https://doi.org/10.1029/2008JF001079 Van Den Eeckhaut, M., Poesen, J., Govers, G., Verstraeten, G., & Demoulin, A. (2007). Characteri of the size distribution of recent and historical landslides in a populated hilly region. <i>Earth and Planetary Science Letters, 256</i> (3), 588-603. https://doi.org/10.1016/j.epsl.2007.01.01 van der Beek, P., & Bourbon, P. (2008). A quantification of the glacial imprint on relief developm in the French western Alps. <i>Geomorphology, 97</i> (1), Article 1. https://doi.org/10.1016/j.geomorph.2007.02.038 von Blanckenburg, F. (2005). The control mechanisms of erosion and weathering at basin scale for cosmogenic nuclides in river sediment. <i>Earth and Planetary Science Letters, 237</i> (3), 462-1238 https://doi.org/10.1016/j.epsl.2005.06.030	, & Lague, D. (2010). Fluvial incision into bedrock: Insights from s and numerical modeling of gorges incising glacial hanging valleys
morphometric analysis and numerical modeling of gorges incising glacial hanging valleys (Western Alps, France). <i>Journal of Geophysical Research: Earth Surface</i> , 115(F2). https://doi.org/10.1029/2008JF001079 Van Den Eeckhaut, M., Poesen, J., Govers, G., Verstraeten, G., & Demoulin, A. (2007). Characteri of the size distribution of recent and historical landslides in a populated hilly region. <i>Earth and Planetary Science Letters</i> , 256(3), 588-603. https://doi.org/10.1016/j.epsl.2007.01.01 van der Beek, P., & Bourbon, P. (2008). A quantification of the glacial imprint on relief developm in the French western Alps. <i>Geomorphology</i> , 97(1), Article 1. https://doi.org/10.1016/j.geomorph.2007.02.038 von Blanckenburg, F. (2005). The control mechanisms of erosion and weathering at basin scale for cosmogenic nuclides in river sediment. <i>Earth and Planetary Science Letters</i> , 237(3), 462-1238 https://doi.org/10.1016/j.epsl.2005.06.030	s and numerical modeling of gorges incising glacial hanging valleys
(Western Alps, France). Journal of Geophysical Research: Earth Surface, 115(F2). https://doi.org/10.1029/2008JF001079 Van Den Eeckhaut, M., Poesen, J., Govers, G., Verstraeten, G., & Demoulin, A. (2007). Characteri of the size distribution of recent and historical landslides in a populated hilly region. Eart and Planetary Science Letters, 256(3), 588-603. https://doi.org/10.1016/j.epsl.2007.01.01 van der Beek, P., & Bourbon, P. (2008). A quantification of the glacial imprint on relief developm in the French western Alps. Geomorphology, 97(1), Article 1. https://doi.org/10.1016/j.geomorph.2007.02.038 von Blanckenburg, F. (2005). The control mechanisms of erosion and weathering at basin scale for cosmogenic nuclides in river sediment. Earth and Planetary Science Letters, 237(3), 462-1238 https://doi.org/10.1016/j.epsl.2005.06.030	
https://doi.org/10.1029/2008JF001079 Van Den Eeckhaut, M., Poesen, J., Govers, G., Verstraeten, G., & Demoulin, A. (2007). Characteri of the size distribution of recent and historical landslides in a populated hilly region. <i>Earth and Planetary Science Letters</i> , 256(3), 588-603. https://doi.org/10.1016/j.epsl.2007.01.01 van der Beek, P., & Bourbon, P. (2008). A quantification of the glacial imprint on relief developmed in the French western Alps. <i>Geomorphology</i> , 97(1), Article 1. https://doi.org/10.1016/j.geomorph.2007.02.038 von Blanckenburg, F. (2005). The control mechanisms of erosion and weathering at basin scale for cosmogenic nuclides in river sediment. <i>Earth and Planetary Science Letters</i> , 237(3), 462-1238 https://doi.org/10.1016/j.epsl.2005.06.030	. Journal of Geophysical Research: Earth Surface, 115(F2).
Van Den Eeckhaut, M., Poesen, J., Govers, G., Verstraeten, G., & Demoulin, A. (2007). Characteri of the size distribution of recent and historical landslides in a populated hilly region. <i>Eart</i> and Planetary Science Letters, 256(3), 588-603. https://doi.org/10.1016/j.epsl.2007.01.01 van der Beek, P., & Bourbon, P. (2008). A quantification of the glacial imprint on relief developm in the French western Alps. <i>Geomorphology</i> , 97(1), Article 1. https://doi.org/10.1016/j.geomorph.2007.02.038 von Blanckenburg, F. (2005). The control mechanisms of erosion and weathering at basin scale for cosmogenic nuclides in river sediment. <i>Earth and Planetary Science Letters</i> , 237(3), 462-1238 https://doi.org/10.1016/j.epsl.2005.06.030	
of the size distribution of recent and historical landslides in a populated hilly region. <i>Earth and Planetary Science Letters</i> , <i>256</i> (3), 588-603. https://doi.org/10.1016/j.epsl.2007.01.01.0133 van der Beek, P., & Bourbon, P. (2008). A quantification of the glacial imprint on relief developm in the French western Alps. <i>Geomorphology</i> , <i>97</i> (1), Article 1. https://doi.org/10.1016/j.geomorph.2007.02.038 von Blanckenburg, F. (2005). The control mechanisms of erosion and weathering at basin scale for cosmogenic nuclides in river sediment. <i>Earth and Planetary Science Letters</i> , <i>237</i> (3), 462-1238 https://doi.org/10.1016/j.epsl.2005.06.030	9/2008JF001079
and Planetary Science Letters, 256(3), 588-603. https://doi.org/10.1016/j.epsl.2007.01.01 van der Beek, P., & Bourbon, P. (2008). A quantification of the glacial imprint on relief developm in the French western Alps. Geomorphology, 97(1), Article 1. https://doi.org/10.1016/j.geomorph.2007.02.038 von Blanckenburg, F. (2005). The control mechanisms of erosion and weathering at basin scale for cosmogenic nuclides in river sediment. Earth and Planetary Science Letters, 237(3), 462-1238 https://doi.org/10.1016/j.epsl.2005.06.030	, J., Govers, G., Verstraeten, G., & Demoulin, A. (2007). Characteristics
van der Beek, P., & Bourbon, P. (2008). A quantification of the glacial imprint on relief developm in the French western Alps. <i>Geomorphology</i> , <i>97</i> (1), Article 1. https://doi.org/10.1016/j.geomorph.2007.02.038 von Blanckenburg, F. (2005). The control mechanisms of erosion and weathering at basin scale for cosmogenic nuclides in river sediment. <i>Earth and Planetary Science Letters</i> , <i>237</i> (3), 462-1238 https://doi.org/10.1016/j.epsl.2005.06.030	of recent and historical landslides in a populated hilly region. Earth
in the French western Alps. <i>Geomorphology</i> , <i>97</i> (1), Article 1. https://doi.org/10.1016/j.geomorph.2007.02.038 von Blanckenburg, F. (2005). The control mechanisms of erosion and weathering at basin scale for cosmogenic nuclides in river sediment. <i>Earth and Planetary Science Letters</i> , <i>237</i> (3), 462-1238 https://doi.org/10.1016/j.epsl.2005.06.030	Letters, 256(3), 588-603. https://doi.org/10.1016/j.epsl.2007.01.040
https://doi.org/10.1016/j.geomorph.2007.02.038 von Blanckenburg, F. (2005). The control mechanisms of erosion and weathering at basin scale for cosmogenic nuclides in river sediment. <i>Earth and Planetary Science Letters</i> , 237(3), 462-1238 https://doi.org/10.1016/j.epsl.2005.06.030	. (2008). A quantification of the glacial imprint on relief development
von Blanckenburg, F. (2005). The control mechanisms of erosion and weathering at basin scale for cosmogenic nuclides in river sediment. <i>Earth and Planetary Science Letters</i> , <i>237</i> (3), 462-1238 https://doi.org/10.1016/j.epsl.2005.06.030	Alps. Geomorphology, 97(1), Article 1.
1237 cosmogenic nuclides in river sediment. <i>Earth and Planetary Science Letters</i> , 237(3), 462-1238 https://doi.org/10.1016/j.epsl.2005.06.030	6/j.geomorph.2007.02.038
1238 https://doi.org/10.1016/j.epsl.2005.06.030	he control mechanisms of erosion and weathering at basin scale from
	n river sediment. Earth and Planetary Science Letters, 237(3), 462-479.
1239 Whipple, K. X. (2001). Fluvial Landscape Response Time : How Plausible Is Steady-State Denudation	6/j.epsl.2005.06.030
	andscape Response Time : How Plausible Is Steady-State Denudation?
1240 <i>American Journal of Science</i> , 301(4-5), 313-325. https://doi.org/10.2475/ajs.301.4-5.313	rience, 301(4-5), 313-325. https://doi.org/10.2475/ajs.301.4-5.313
Wood, J. L., Harrison, S., & Reinhardt, L. (2015). Landslide inventories for climate impacts research	nhardt, L. (2015). Landslide inventories for climate impacts research in
the European Alps. <i>Geomorphology</i> , 228, 398-408.	omorphology, 228, 398-408.
1243 https://doi.org/10.1016/j.geomorph.2014.09.005	
Zachos, J., Pagani, M., Sloan, L., Thomas, E., & Billups, K. (2001). Trends, Rhythms, and Aberration	6/j.geomorph.2014.09.005
1245 Global Climate 65 Ma to Present. <i>Science</i> , <i>292</i> (5517), 686-693.	
1246 https://doi.org/10.1126/science.1059412	, Thomas, E., & Billups, K. (2001). Trends, Rhythms, and Aberrations in





1247	Zech, R., Zech, M., Kubik, P. W., Kharki, K., & Zech, W. (2009). Deglaciation and landscape history
1248	around Annapurna, Nepal, based on 10Be surface exposure dating. Quaternary Science
1249	Reviews, 28(11), 1106-1118. https://doi.org/10.1016/j.quascirev.2008.11.013
1250	Zerathe, S., Lebourg, T., Braucher, R., & Bourlès, D. (2014). Mid-Holocene cluster of large-scale
1251	landslides revealed in the Southwestern Alps by 36Cl dating. Insight on an Alpine-scale
1252	landslide activity. Quaternary Science Reviews, 90, 106-127.
1253	https://doi.org/10.1016/j.quascirev.2014.02.015
1254	Zhang, T., Li, D., East, A. E., Walling, D. E., Lane, S., Overeem, I., Beylich, A. A., Koppes, M., & Lu, X
1255	(2022). Warming-driven erosion and sediment transport in cold regions. Nature Reviews
1256	Earth & Environment, 3(12), 832-851. https://doi.org/10.1038/s43017-022-00362-0
1257	
1258	